# Grid Oscillators

Thesis by
Zoya Basta Popović

In Partial Fulfillment of the Requirements
for the Degree of
Doctor of Philosophy

California Institute of Technology
Pasadena, California

1990

(Submitted May 2, 1990)

To my family with love

## Acknowledgements

I wish to thank my advisor David Rutledge for his enthusiasm which attracted me to microwaves and electromagnetics. Thanks for the knowledge and ideas he shared with us, for teaching me how to approach the world of research, and for the times we spent talking as friends. I consider myself privileged to be one of his students.

I also wish to thank my fellow graduate students Bobby Weikle, Moonil Kim, Karen Lee, Scott Wedge, Yong Guo, Jon Hacker, as well as Dr. Phil Stimpson, Dr. Wyman Williams, Professor Rick Compton, Dale Yee and Kent Potter for many useful conversations and the good times we spent together. Many thanks to my friends Svetlana Tatić, Suzana and Tim Brown, Dana Stevanović, Gabriel Rebeiz, Craig Leff, Dayalan Kasilingam and David Schweizer for being there when I needed them, and for making my years in graduate school more pleasant.

This work would not have been possible without the love and advice of my parents, who showed me that hard work can be fun and rewarding. I am also dedicating this work to my grandmothers and to the memory of my grandfathers, who encouraged me to leave my country to continue my education and gave me much valuable and wise advice. Thanks to my dear sisters for all the love and good humor, with the hope that their work will be as exciting and as rewarding. Affectionately, I thank my husband Srdjan Basta for his love and patience.

## Grid Oscillators

### Abstract

In the microwave and millimeter-wave frequency range, solid-state oscillators have limited output power levels. The alternative high-power sources are tubes, which are expensive, bulky, have a limited lifetime and require high-voltage power supplies. Combining a large number of low-power solid-state negative resistance devices becomes attractive. In this work a coherent oscillator that can combine thousands of solid-state devices is presented. The feasibility of a reliable high-power, monolithically integrated microwave and millimeter-wave source is demonstrated. In this approach, the active devices load a two-dimensional metal grid that radiates, and the power combining is done in free-space. Several MESFET grid oscillator designs are presented in this thesis, ranging from a 5 by 5 to a 10 by 10 grid in size. The 100-MESFET hybrid grid oscillator is a planar structure suitable for wafer-scale monolithic integration. This grid locks at 5 GHz, with an ERP of 24 Watts and a conversion efficiency of 20%. An equivalent embedding circuit for the devices in the grid predicts the oscillation frequency. The devices in the grid self-lock with no external locking signal present, but the grid can also be externally injection-locked. Measurements and analysis are presented for the injection-locked planar grid oscillator.

## Contents

# Chapter 1

## Introduction

The frequency range from 30 GHz to 300 GHz is usually called the millimeter-wave region. These frequencies have applications in radio-astronomy, communication, radar, radiometry, remote sensing, plasma diagnostics and spectroscopy [1]. The effects of the atmosphere on wave propagation are important for most of these applications. The earth's atmosphere absorption spectrum has minima, or windows, in the millimeter-wave region around 35 GHz, 93 GHz, 130 GHz and 225 GHz. Millimeter waves propagate through dust, fog, smoke and clouds, making them attractive for radar used in adverse environmental conditions. These frequencies also pass through interstellar gases and dust. This is important for radio-astronomy [2], since many phenomena, such as star birth, occur deep within regions of space through which optical telescopes cannot penetrate. Recently there has been a lot of interest in the earth's ozone layer, and most of the chemicals in the ozone cycle have absorption lines in the millimeter and submillimeter-wave range. The high millimeter-wave frequencies have some advantages over microwave frequencies. For a given beamwidth and gain, millimeter-wave antennas are very small. They also offer wide bandwidths for communication applications.

## 1.1 Microwave and Millimeter-wave Sources

One of the key components in every millimeter-wave system is the oscillator, whether it is the high-power source for a radar transmitter, or a low-power local-oscillator for a radio-astronomy receiver. Two types of sources have been used so far : tubes (TWT, BWO, klystron, magnetron, carcinotron, gyrotron) and solid-state devices. The latter can be two terminal devices, such as the IMPATT and Gunn diodes, or three terminal transistors, such as the MESFET (Metal Semiconductor Field Effect Transistor), HEMT (High Electron Mobility Transistor), or HBT (Heterojunction Bipolar Transistor). Tubes are high-power sources and have higher efficiencies than the semiconductor devices. For example, gyrotrons have achieved hundreds of kilowatts CW with efficiencies close to 50%. The output powers of individual solid-state devices and tubes versus frequency

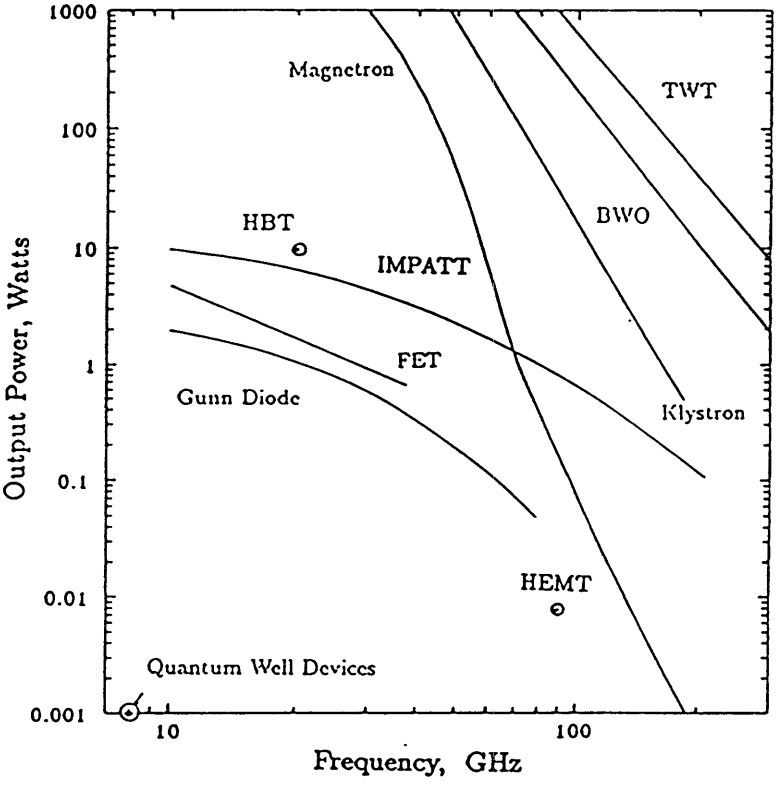


**Fig. 1.** Comparison of output power levels of solid-state and tube sources in the microwave and millimeter-wave region.

are given in Fig. 1. Solid-state technology is continually improving. Recent efforts in HEMT devices [3] have resulted in a 23% power-added efficiency at 93 GHz with an output power of 18 mW. HBT's [4] have promising high-power applications with good yields and power-added efficiencies of 40% at 12 GHz with output powers of 10 W. Quantum-well devices have pushed the frequency limit to 420 GHz [5], with an output power of 200 nW. The individual output power levels from solid-state devices are still low compared to tubes at the millimeter-wave end. However, their advantages give motivation for finding a way to get enough power from them to replace tubes. The most obvious applications are any space or airborne systems, since tubes require large DC power supplies and have a short lifetime, typically on the order of several hundred hours. In addition, solid-state devices are relatively inexpensive with the existing integrated-circuit technology.

## 1.2 Power Combining

A way of obtaining high power from semiconductor devices is to combine the outputs of several devices coherently. Most power-combining schemes so far [6],[7] involve placing a few (up to 12) devices in a waveguide cavity (Fig. 2a) and locking to an external injection signal. Pulsed IMPATT diodes have given 20, 40 and 48 Watts peak power from 2,4 and 6 rectangular waveguide modules respectively, where each device could deliver 10 to 13 W [8]. Eight CW IMPATT's were combined in a cylindrical cavity with a dominant $TM_{010}$ mode and an output power of 10 W at 35 GHz. Up to 4 InP Gunn diodes were combined [9] at 90 GHz, with combining efficiencies reaching 106%.

Waveguide cavity power combiners become impractical at higher frequencies because of the losses in the metal walls and the small guide dimensions. Some free-space combining work has been done with two InP Gunn diodes in a spherical mirror resonator [10] (Fig. 2b), as well as with three IMPATT's feeding patch antennas [11], but in all these examples each device had its own biasing and tuning circuit. This is not practical if a large number of devices, for example a thousand, is to be combined.

This work describes a way to quasi-optically combine the output powers of a large number of semiconductor oscillators by loading a two-dimensional metal grid with active devices. The grid structure is convenient for both two- or three-terminal device. The experimental grids demonstrated in this work are hybrid MESFET circuits combining up to one hundred devices between 3 and 10 GHz. All the devices share one biasing circuit. They are spatially coupled through a Fabry-Perot cavity.

Fig. 3 shows the dependence of the output power of some solid-state devices versus frequency [13], and in the millimeter-wave range it is a $\frac{1}{f^2}$ dependence. This means that in order to flatten out this curve at higher frequencies, a source

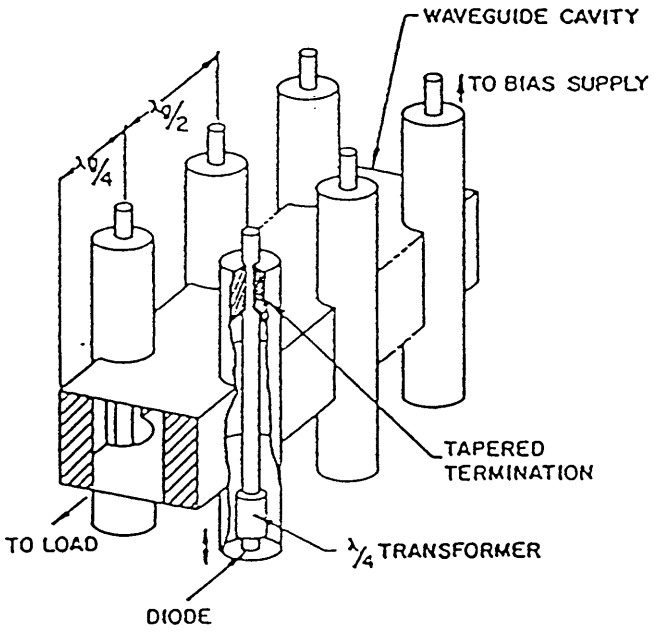


(a)

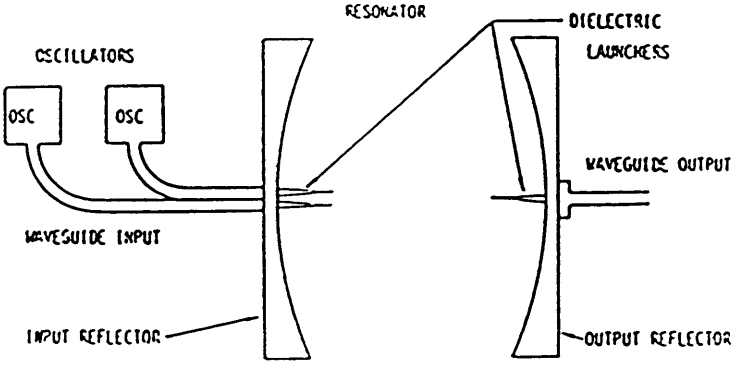


(b)

**Fig. 2** (a) IMPATT diode X-bad waveguide combiner [6]. (b) Quasi-optical power combining of two InP Gunn-diodes at 60 GHz [9].

for which the power would grow as the square of the frequency is needed. Any two-dimensional structure is a good candidate, and this was one of the motivations for using a planar grid structure.

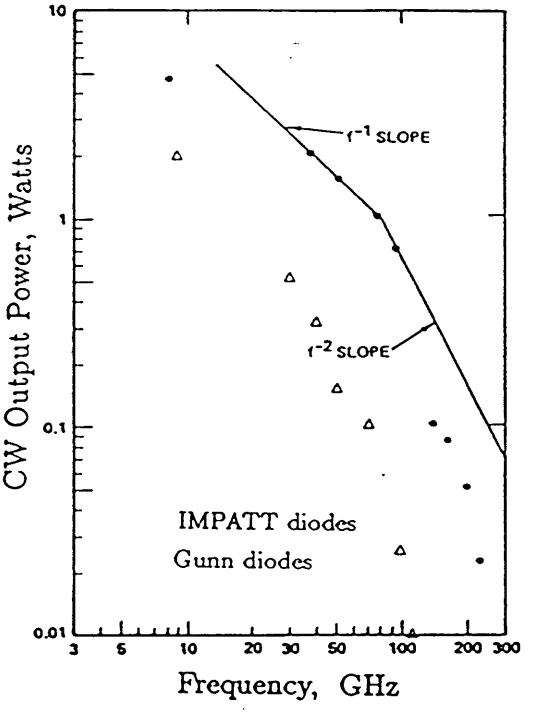


Fig. 3. Dependence of output power versus frequency for IMPATT and Gunn diodes [12].

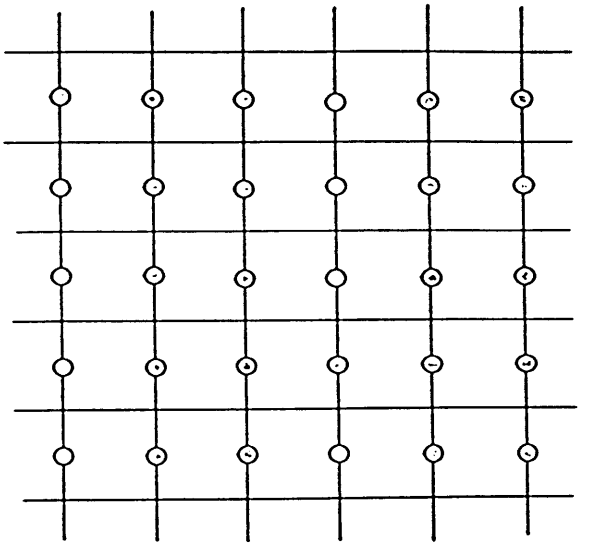

Fig. 4. Schematic of a grid loaded with negative resistance devices.

The **grid oscillator** can be made monolithically on a single wafer and scaled to as high a frequency as the one at which the devices can oscillate at. Possible designs for monolithic grids at 30 to 90 GHz will be presented in the last chapter. The grids are planar, light weight, small volume, easily biased, and offer a large variety of applications.

A schematic of a grid oscillator is shown in Fig. 4. If the grid is several free-space wavelengths across, and if the devices are a fraction of a wavelength apart, one can look at this grid as a continuous, uniform, active sheet. If the devices in the grid locked in phase, the radiated wave is a plane wave, which allows simple transmission-line analysis.

## 1.3 Organization of the Thesis

The thesis describes several grid oscillators that were tested and analyzed. Parts of this work have been published in the articles [15], [16], and [17]. The first working hybrid 25-MESFET grid is described in Chapter 2. This grid proved that the grid oscillator concept works.

The 36-MESFET bar grid is presented in Chapters 3 and 4. The theoretical analysis and simulations of this oscillator are based on the symmetry of an infinite loaded grid. The analysis predicts the oscillation frequency and gives an equivalent transmission-line circuit for the transistors in the grid, which makes it possible to design the oscillator. The measurements on the bar-grid oscillator are presented in Chapter 4.

One of the most important ideas behind the grid oscillators is the fact that they can potentially be monolithically integrated on a single wafer. The grids described in Chapters 2-4 were not planar in the real sense. In Chapter 5 is presented a planar version of the oscillator with 100 MESFET's at 5 GHz.

The grid oscillators lock without an external signal present. However, for some applications it would be advantageous to lock the high-power grid to a low-power external oscillator. The injection-locking behaviour of the planar grid oscillator is described in Chapter 6. A general theory for injection-locked oscillators is also presented, and some measurements made to confirm the results.

In the last chapter are given some possible grid designs for wafer-scale integrated grids, which assume currently existing devices and available technology. The grid oscillator is an antenna as well as a source, and several potential applications that will be subjects of future work are described.

## References

[1] J.C. Wiltse, "Introduction and Overview of Millimeter Waves," *Infrared and Millimeter Waves, Vol.4,* Academic Press Inc., 1981, pp. 1–18.

[2] J. D. Kraus, *Radio Astronomy,* Cygnus-Quasar Books, 2nd Edition.

[3] M. Kao, P. M. Smith, P. Ho, P. Chao, K. H. G. Duh, A. A. Jabra, J. M. Ballingall, "Very High Power-Added Efficiency and Low-Noise 0.15-$\mu$m Gate-Length Pseudomorphic HEMT's," *IEEE Electron Device Letters, Vol. 10, N0. 12,* 580–582, December 1989.

[4] P. M. Asbeck, M. F. Chang, K. C. Wang, D. L. Miller, G. J. Sullivan, N. H. Sheng, E. Sovero, J. A. Higgins, "Heterojunction Bipolar Transistors for Microwave and Millimeter-Wave Integrated Circuits," *IEEE Trans. on Microwave Theory and Techniques, Vol. MTT-35,* 1462–1470, December 1987.

[5] E. R. Brown, T. C. L. G. Sollner, C. D. Parker, W. D. Goodhue, C. L. Chen, "Oscillations up to 420 GHz in GaAs/AlAs Resonant Tunneling Diodes," *Applied Physics Letters, Vol. 55, No 17,* 1777–1779, October 1989.

[6] K. J. Russel, "Microwave Power Combining Techniques," *IEEE Transactions on Microwave Theory and Techniques, Vol. MTT-27,* 472–478, May 1979.

[7] K. Chang, C. Sun, "Millimeter-Wave Power Combining Techniques," *IEEE Transactions on Microwave Theory and Techniques, Vol. MTT-31,* 91–107, February 1983.

[8] K. Chang, R. L. Ebert, "W-Band Power Combiner Design ," *IEEE Transactions of Microwave Theory and Techniques, Vol. MTT-28,* 295, April 1980.

[9] J. J. Sowers, J. D. Crowley, F. B. Fank, "CW InP Gunn Diode Power Combining at 90 GHz," *IEEE MTT Symposium Digest,* 503, Dallas, 1982.

[10] L. Wandinger, V. Nalbandian, "Millimeter-Wave Power Combiner Using Quasi-Optical Techniques," *IEEE Transactions on Microwave Theory and Techniques, Vol. MTT-34,* 273–279, February 1983.

[11] R. Dinger, D. White, D. Bowling, "A 10-GHz Space Power Combiner with Parasitic Injection Locking," Naval Weapons Center Technical Publication 6704, March 1986.

[13] H. J. Kuno, "IMPATT Devices for Generation of Millimeter Waves," *Infrared and Millimeter Waves, Vol. 1,* 1979, pp. 96.

[14] N. B. Kramer, "Sources of Millimeter Wave Radiation: Travelling-Wave Tube and Solid-State Sources," *Infrared and Millimeter Waves, Vol.4,* Academic Press Inc., 1981, pp. 151–197.

[15] Z. B. Popović, M. Kim, D. B. Rutledge, "Grid Oscillators," *International Journal of Infrared and Millimeter Waves, Vol. 9, No. 7,* July 1988, pp. 647–654.

[16] Z. B. Popović, R. M. Weikle, M. Kim, K. A. Potter, D. B. Rutledge, "Bar-Grid Oscillators," *IEEE Trans. on Microwave Theory and Techniques, Vol. MTT-38, No. 3,* March 1990, pp. 225–230.

[17] Z. B. Popović, R. M. Weikle II, M. Kim, D. B. Rutledge, "Planar Grid Oscillators," *submitted for publication to the IEEE Transactions on Microwave Theory and Techniques,* April 1990.

# Chapter 2

## A 25-MESFET Hybrid Grid Oscillator

The grid oscillator configuration [1] is shown in Fig. 2.1. A metal grid is loaded with solid-state negative resistance devices. The grid can be on a dielectric substrate. It is placed between a metal mirror and another dielectric slab, which acts as a partially transparent reflector. The mirror and the dielectric slab form a Fabry-Perot cavity. The devices lock to a mode of the cavity.

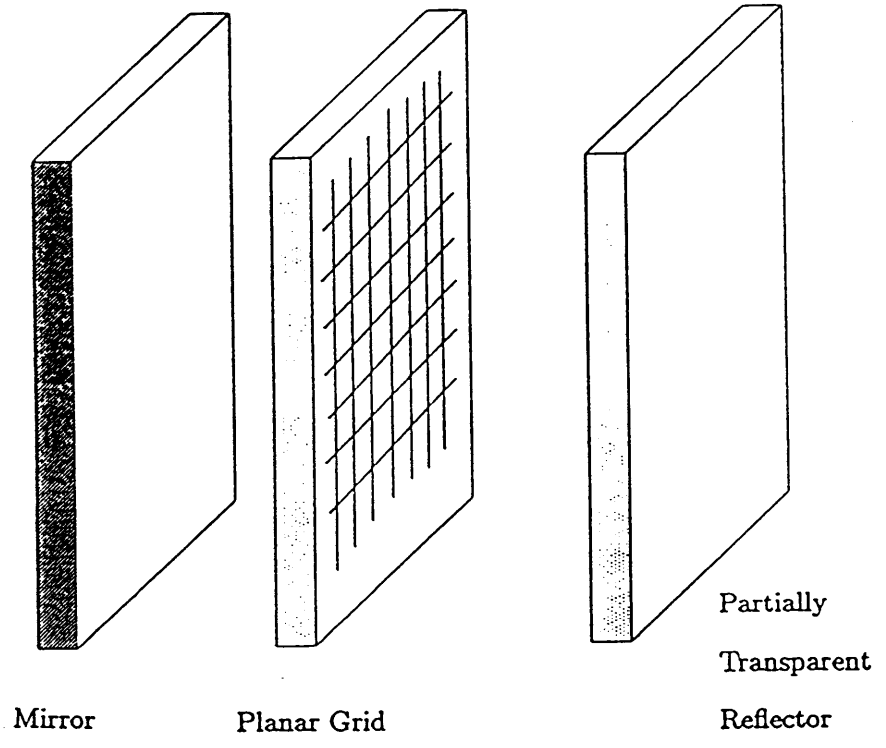


**Fig. 2.1.** The grid oscillator configuration.

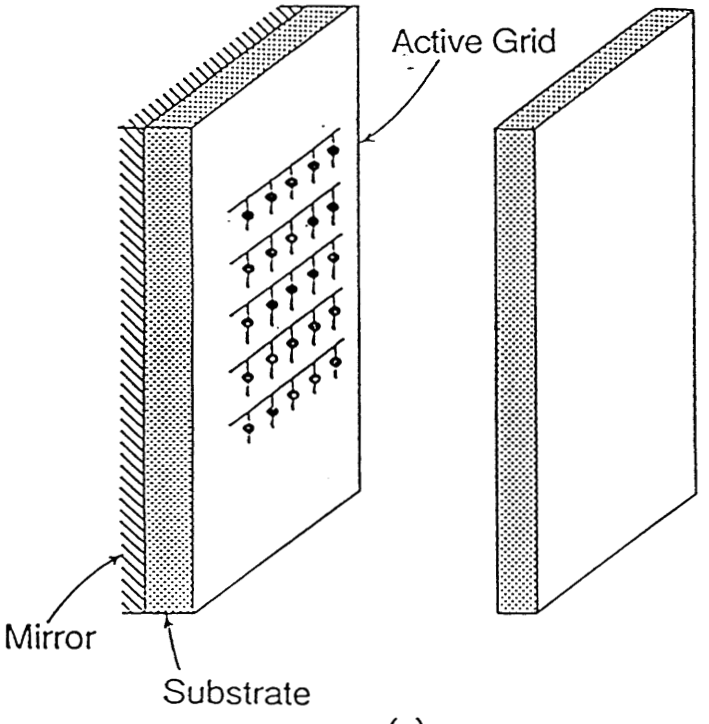


(a)

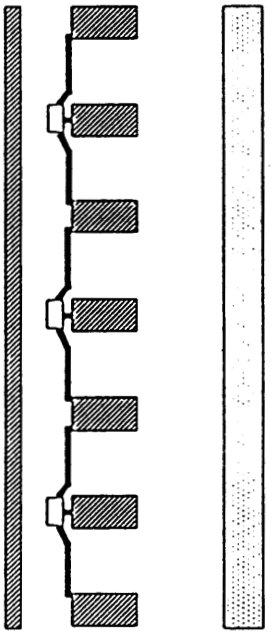

(b)

Fig. 2.2. (a) 5 by 5 MESFET grid, and the *bar-grid oscillator* (b).

Several different hybrid grid oscillators were made, measured and analyzed. The first working MESFET oscillator was a 5 by 5 array at 10 GHz [2], shown schematically in Fig. 2.2a. The grid is etched on a quarter dielectric wavelength thick grounded microstrip Duroid substrate. The ground plane of the substrate acts as the mirror, and another Duroid slab, with copper etched away from both sides, is placed in front of the grid as the partially transparent reflector. The mirror position in this case is fixed, so that there can be no mirror-tuning.

The second MESFET grid oscillator, shown in Fig. 2.2b, eliminated the dielectric substrate. This grid will from now on be called the *bar-grid oscillator*, since 36 devices are soldered directly onto a stack of metal bars. The bars provide excellent heat-sinking and DC bias, and they act as a partially transparent reflector as well. This grid oscillates around 3 GHz. It does not require the dielectric slab shown in Fig. 2.2b to lock. However, two slabs were used in the measurements for impedance-matching. In this oscillator the mirror can be translated for mechanical tuning, and electrical tuning can be obtained by modulating the gate or the drain bias.

The third hybrid grid oscillator was a *planar* 100-MESFET oscillator at 5 GHz, as shown in Fig. 2. 1. This grid is made on a dielectric substrate, and the mirror position can be changed. The grid itself is the partially transparent reflector. This grid demonstrates the possibility of wafer-scale, monolithically integrated, high-power grid oscillators.

## 2.1 The 5 by 5 MESFET grid oscillator

The 5 by 5 MESFET grid is shown in Fig. 2.3. The devices are Fujitsu MESFET's (FSC11), made for satellite receivers at 4 GHz. These devices usually give about 20 mW in single-transistor microstrip oscillators. The substrate is a microstrip substrate *Duroid*, with a dielectric constant $\epsilon_r = 10.5$, and 2.35 mm thick, which is a quarter of a dielectric wavelength at 10 GHz.

Fig. 2.4 shows the orientation of the transistor leads in the grid. The vertical lines connected to the transistor drain and gate terminals support the flow of RF currents, and the radiated electric field vector is parallel to them. The horizontal lines are used for DC bias, and they should not affect the RF fields. This was confirmed by cross-polarization measurements. The grid dimensions have been chosen by experiment, and the period of the array is 13 mm. The gate lead is not connected to a DC bias. Its length (5 mm) is chosen so that the RF embedding impedance for the gate is inductive. The horizontal drain tabs, which are 3.5 mm

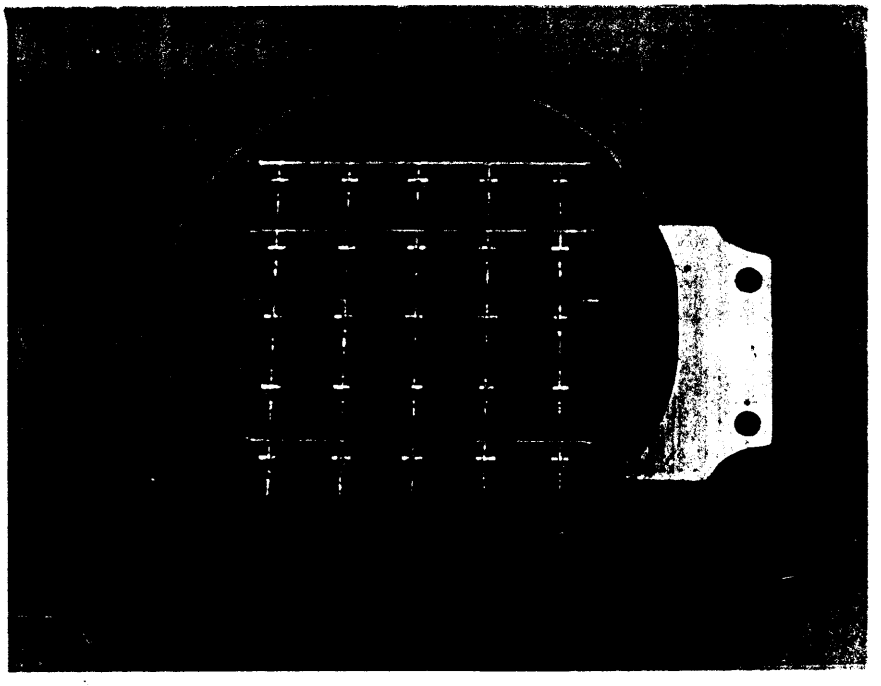

**Fig. 2.3.** Photograph of the 25-transistor oscillator grid at 9.7 GHz.

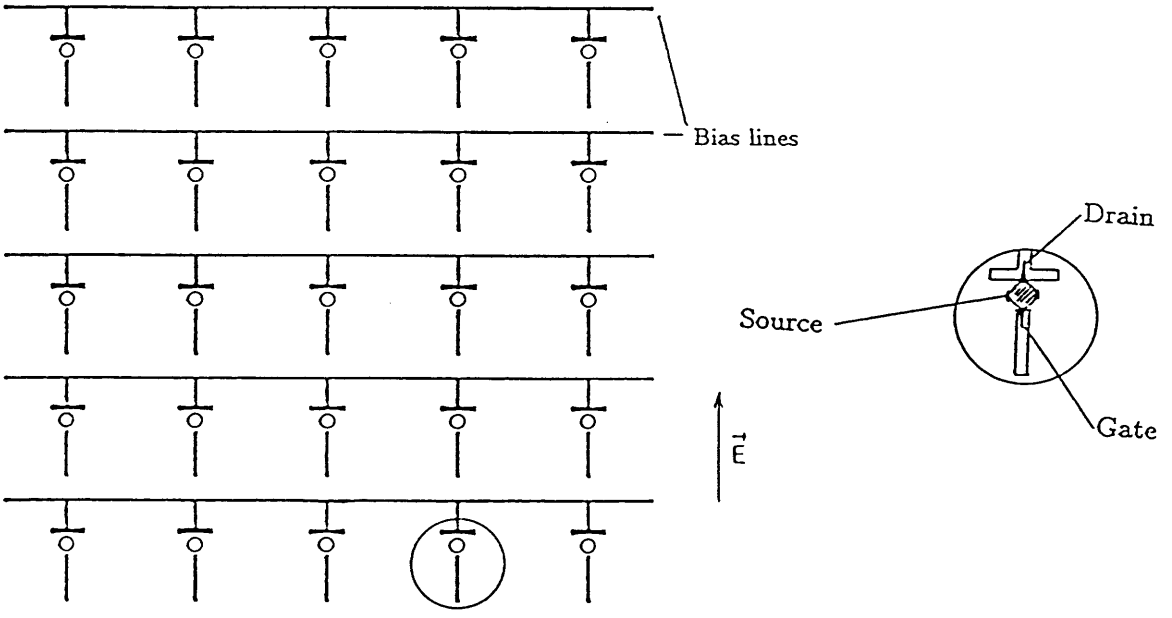


Fig. 2.4. The 5 by 5 MESFET grid oscillator layout.

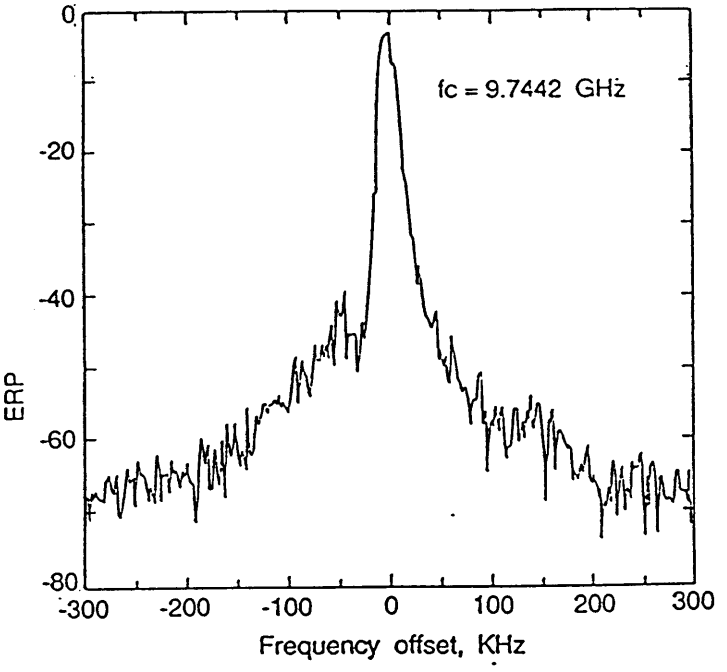


Fig. 2.5. Spectrum of locked 25-MESFET grid

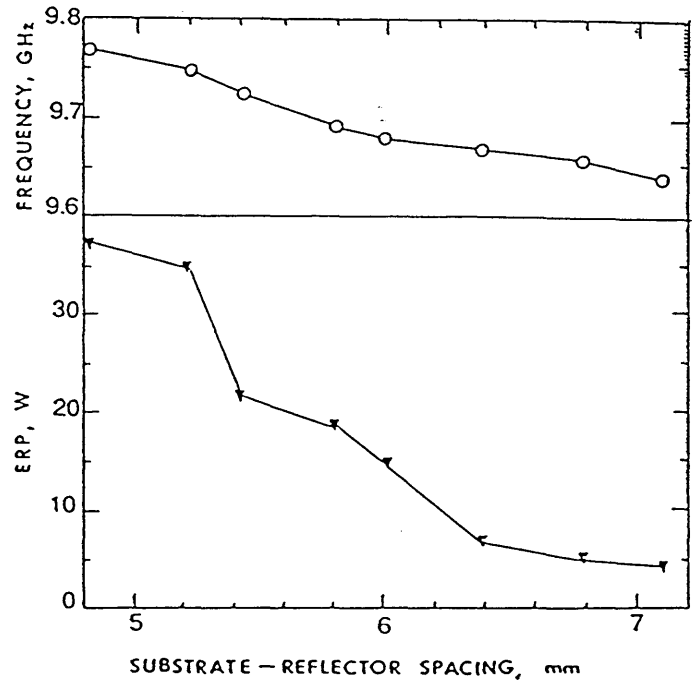


Fig. 2.6. The radiated power and oscillation frequency vs. substrate-reflector spacing.

long, are chosen empirically, and they help in matching the impedance of the device, since the power drops when they are removed.

When biased at a drain voltage of 4 V, the grid oscillates at 9.7 GHz. The spectrum is shown in Fig. 2.5. Varying the spacing between the substrate and the reflector shifts the frequency over a 1% range, and produces large changes in the power, as shown in Fig. 2.6. The largest measured effective radiated power relative to an isotropic source (ERP) is 37 W at a spacing of 4.8 mm. Fig. 2.7 shows the measured far-field pattern where the peak ERP was 20.7 watts. Instabilities caused by reflections prevented pattern measurements at the higher power levels. From the measured pattern, we can deduce the total radiated power, which is 464 mW. This is roughly 25 times the power that we typically get from a single transistor oscillator. The DC to RF conversion efficiency is 14.5%.

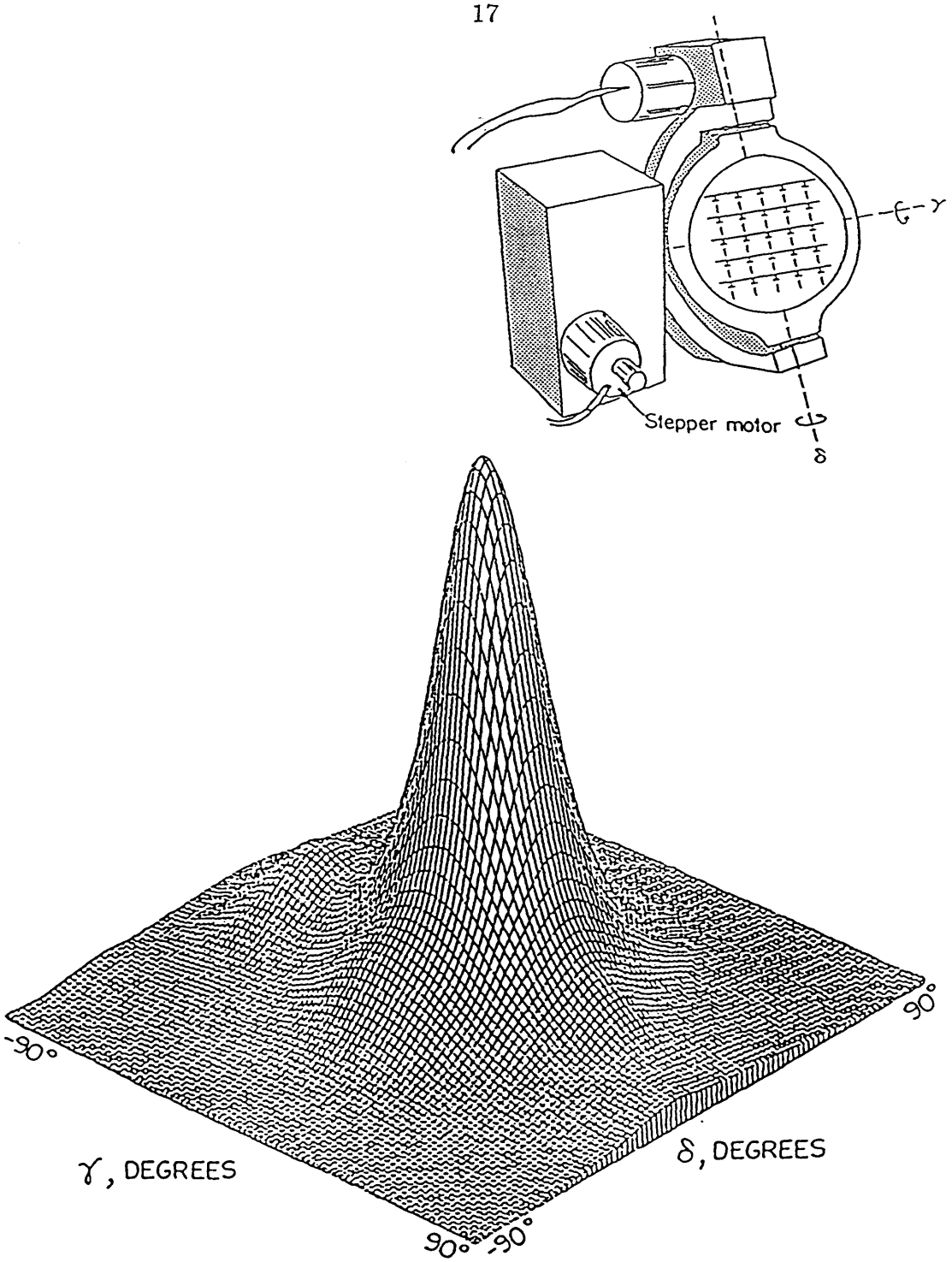


Fig. 2.7. Two-dimensional far-field pattern of the transistor grid. The vertical scale is linear in power, the peak ERP is 20.7 W, and the directivity is 16.4 dB. The angles $\gamma$ and $\delta$ are indicated on the measurement setup shown in the upper right-hand corner of the figure. The E-plane pattern is a scan of $\gamma$ with $\delta = 0$, and the H-pane pattern is a scan of $\delta$ with $\gamma = 0$.

## 2.2 Calculating the Grid Far-field Pattern

If we assume that the grid is infinite and that the devices are locked in phase, we can treat each transistor as a current source feeding a short dipole antenna. The dipole is on top of an infinite grounded dielectric, and above it is an air gap and a dielectric superstrate. The far field of such a dipole can be found by reciprocity [3,4]. A test dipole in the far-field will produce a field at the dielectric substrate surface. If the test dipole moves along the E-plane of the grid, as shown in Fig. 2.8a, the incident field on the grid surface will be the same as the grid E-plane pattern, by reciprocity. Since the test dipole is in the far field, plane-wave analysis can be used. The equivalent transmission-line circuit is shown in Fig. 2.8b. The pattern is proportional to the square of the transmission coefficient at the plane of the grid:

$$P(\theta,\phi) \propto |\tau(\theta,\phi)|^2 = \left|\frac{E_{substrate}}{E_{air}}\right|^2 = \left(Y_0 \frac{V}{I}\right)^2,$$

where $Y_0$ is the free-space admittance. The TM incident wave gives the E-plane, and the TE incident wave gives the E-plane for a single dipole in the grid. The total grid pattern is found by assuming an array factor for which all transistors are equal current sources. The theoretical and measured patterns are shown in Fig. 2.9. The measured E-plane in Fig. 2.9a is shifted about 7 degrees, and the reason is a tilt in the dielectric slab with respect to the grid, which introduces a linear phase shift across the plane of the grid.

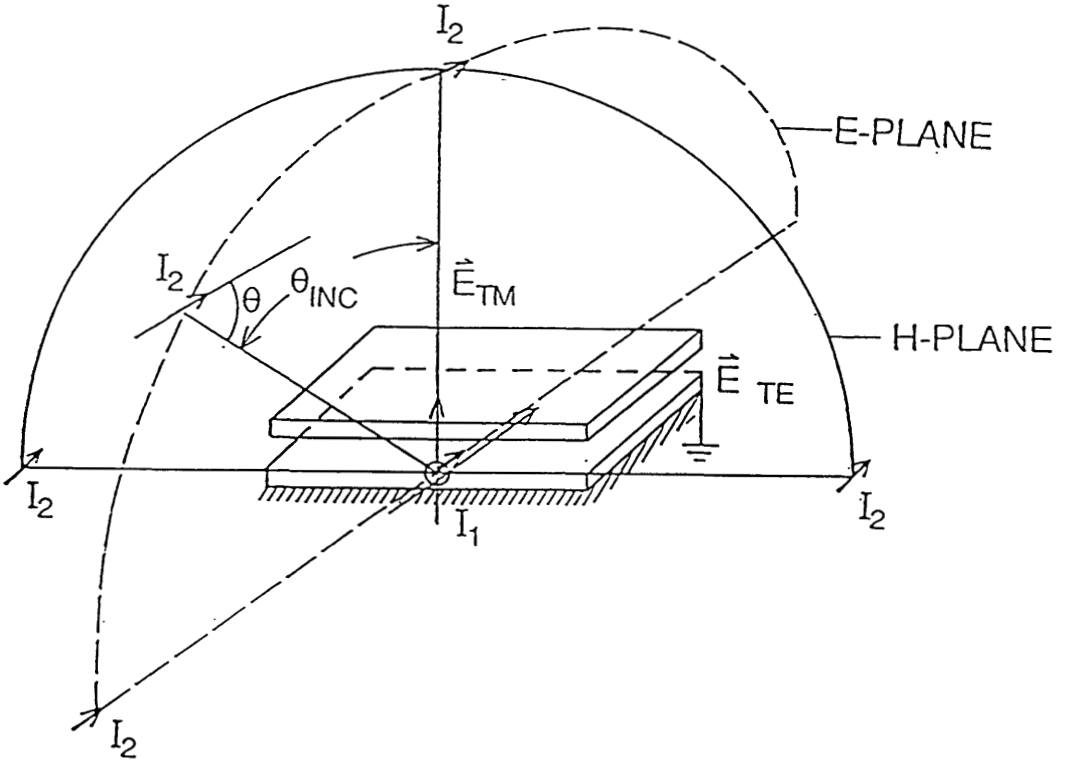


(a)

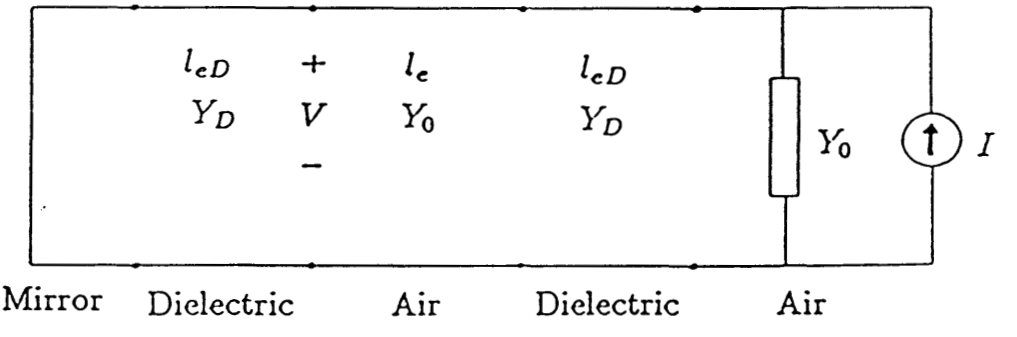


(b)

Fig. 2.8. (a) The pattern of the grid is found by reciprocity. The fields of a test dipole are found as it is moved along the E and H planes. (b) Equivalent transmission-line circuit for calculating the far-field pattern of the grid. The TM polarization gives the E-plane, and the TM polarization the H-plane. The corresponding impedances in each of the layers are $Y_{TM} = Y_0\sqrt{\epsilon_r}/\cos\theta$, $Y_{TE} = Y_0\sqrt{\epsilon_r}\cos\theta$, and the electrical length of each of the layers is $l_e = \sqrt{\epsilon_r}d\cos\theta$.

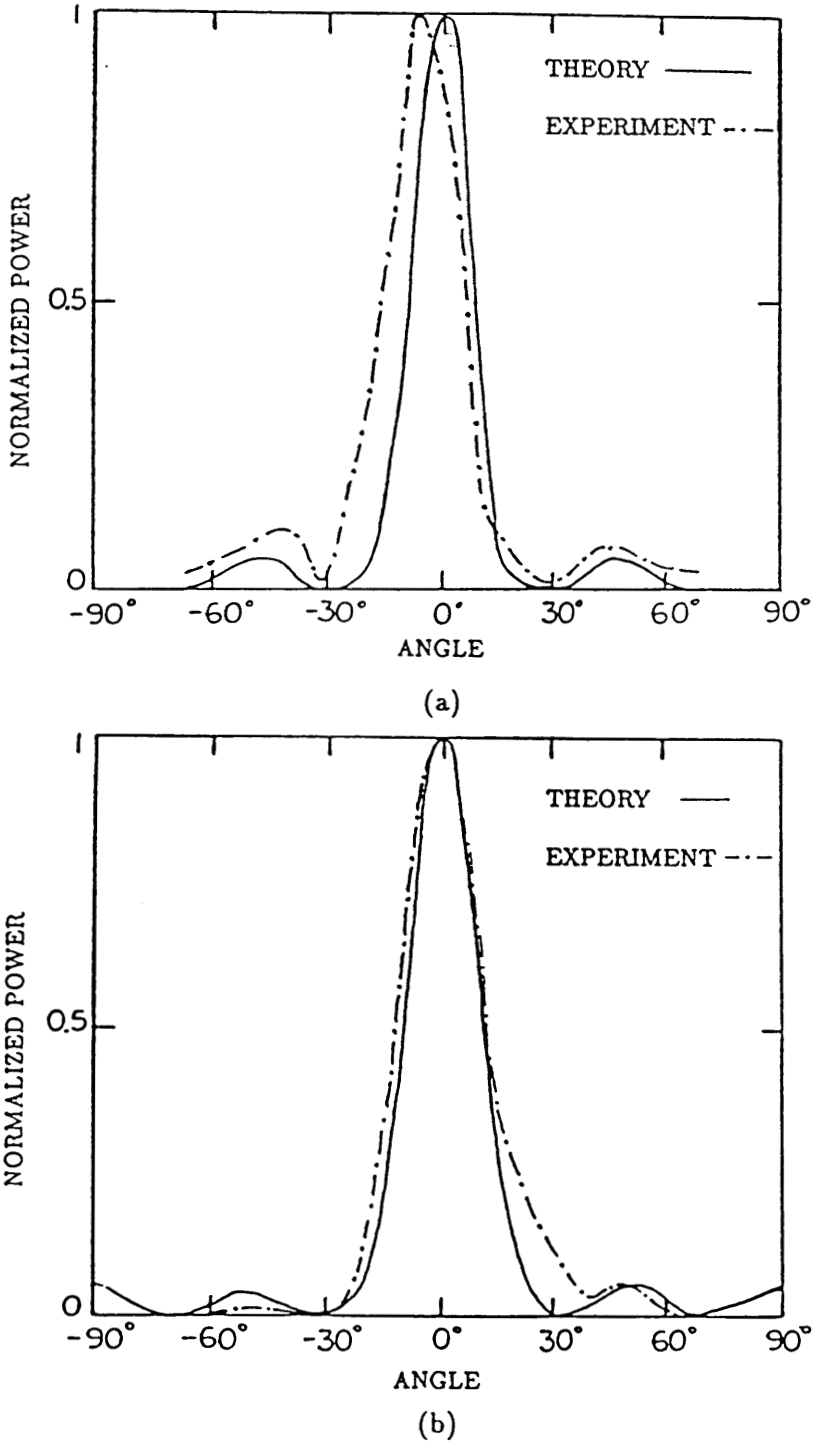


Fig. 2.9. (a) E-plane, (b) H-plane of transistor grid, theory and experiment. The scale is linear in power.

## References

[1] Z. B. Popović, D. B. Rutledge, "Diode-Grid Oscillators," *1988 IEEE Antennas and Propagation Symposium*, Syracuse, New York, June 1988.

[2] Z. B. Popović, M. Kim, D. B. Rutledge, "Grid Oscillators," *International Journal of Infrared and Millimeter Waves, Vol. 9, No. 7,* 647–654, July 1988.

[3] D. B. Rutledge, D. P. Neikerk, D.P. Kasilingam, "Integrated Circuit Antennas," *Infrared and Millimeter-Waves, Vol. 10,* 1–87, 1983.

[4] H. Y. Yang, N. G. Alexópoulos, "Gain Enhancement Methods for Printed Circuit Antennas Through Multiple Superstrates", *IEEE Transactions on Antennas and Propagation, Vol. 35, No. 7,* July 1987.

# Chapter 3

## The Bar-Grid Oscillator — Theory

The side view of the bar-grid oscillator is shown in Fig. 3.1. It is a 6 by 6 grid. The devices (Fujitsu FSC11) are soldered directly onto a stack of metal bars. The bars provide excellent heat-sinking and bias connections. Adjacent rows of the grid share gate and drain bias bars to minimize the number of bias lines, as shown in Fig. 3.2. The grid is $0.6\,\lambda_0$ across, and the period is 10 mm ($\lambda_0/10$).

The 5 by 5 grid described in Chapter 2 demonstrated the locking and the pattern was predicted. However, it is very hard to find the impedances presented at the device terminals in the grid. The dielectric is thick, and the source leads pass through it, so that the devices couple strongly through the substrate. The substrate modes have been calculated for two dipoles and slots [1], but the calculations would be considerably more complicated for 25 antennas. The goal was to make a grid oscillator structure for which the impedances presented to the devices could be calculated, and optimized for high-power output. The first step was to make a structure where all the currents were in one plane. The dielectric substrate was left out for heat-sinking purposes.

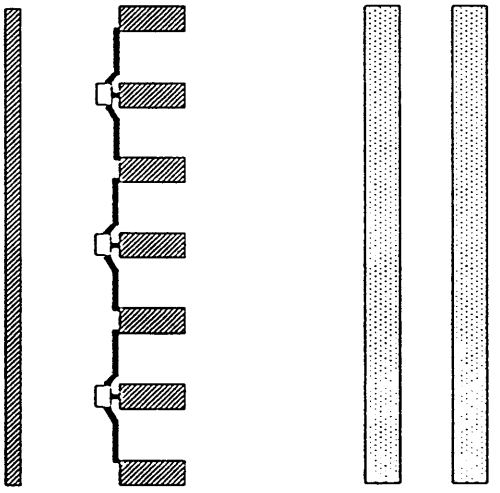

Fig. 3.1. Side view of the MESFET bar-grid oscillator.

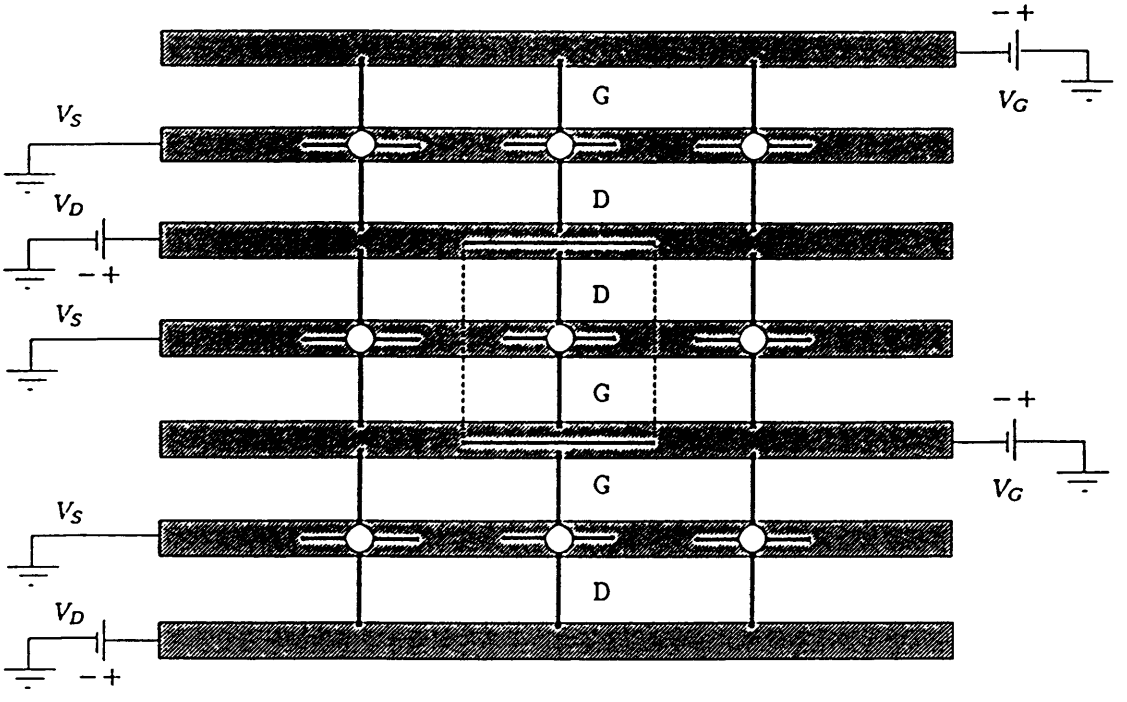


Fig. 3.2. Boundary conditions on the symmetry lines define the unit cell. The solid lines on top and bottom represent electric walls, and the dashed lines on the sides magnetic walls. Adjacent rows share drain and gate biases.

## 3.1 Unit Waveguide

The goal of the analysis presented here is to find the reflection coefficient of an infinite grid for a plane wave at normal incidence. Strictly speaking, this analysis should be accurate only for grids that are much larger than a free-space wavelength. The symmetry of the grid imposes boundary conditions, which define a unit cell [2], shown in Fig. 3.2. This reduces the problem of analyzing the grid to that of analyzing an equivalent waveguide. The equivalent waveguide has electric walls (tangential electric field is zero) on the top and bottom, magnetic walls (tangential magnetic field is zero) on the sides, and extends in the $+z$ and $-z$ directions, with the transistors in the $z = 0$ plane.

In order to model the behavior of the transistors in the grid, the impedances presented at the device terminals need to be found. The propagating mode has a real wave impedance and can be modeled with a TEM transmission line. The reactive impedances arise from the coupling between the currents in the leads and the evanescent modes. The method used to find these mode impedances is dual to the EMF analysis in the paper by Eisenhart and Kahn [3] for a post in a rectangular waveguide. Our problem is different, since there are two waveguides in the unit cell as shown in Fig. 3.3 (side view) and Fig. 3.4 (front view). This introduces an additional mutual capacitance and inductance, which can be found by considering the odd and even combinations of the currents and voltages, shown in Fig. 3.3.

For example, when both the drain and the gate current are flowing into the transistor (Fig. 3.4a), the tangential magnetic fields cancel at the symmetry plane in the middle of the source bar, so we can place a magnetic wall (Fig. 3.4b). The currents and the fields are expanded in terms of the waveguide modes. Since the transistor leads are short compared to a wavelength, the currents are assumed to be uniform in the $x$ and $y$ directions. The total inductance for this case is:

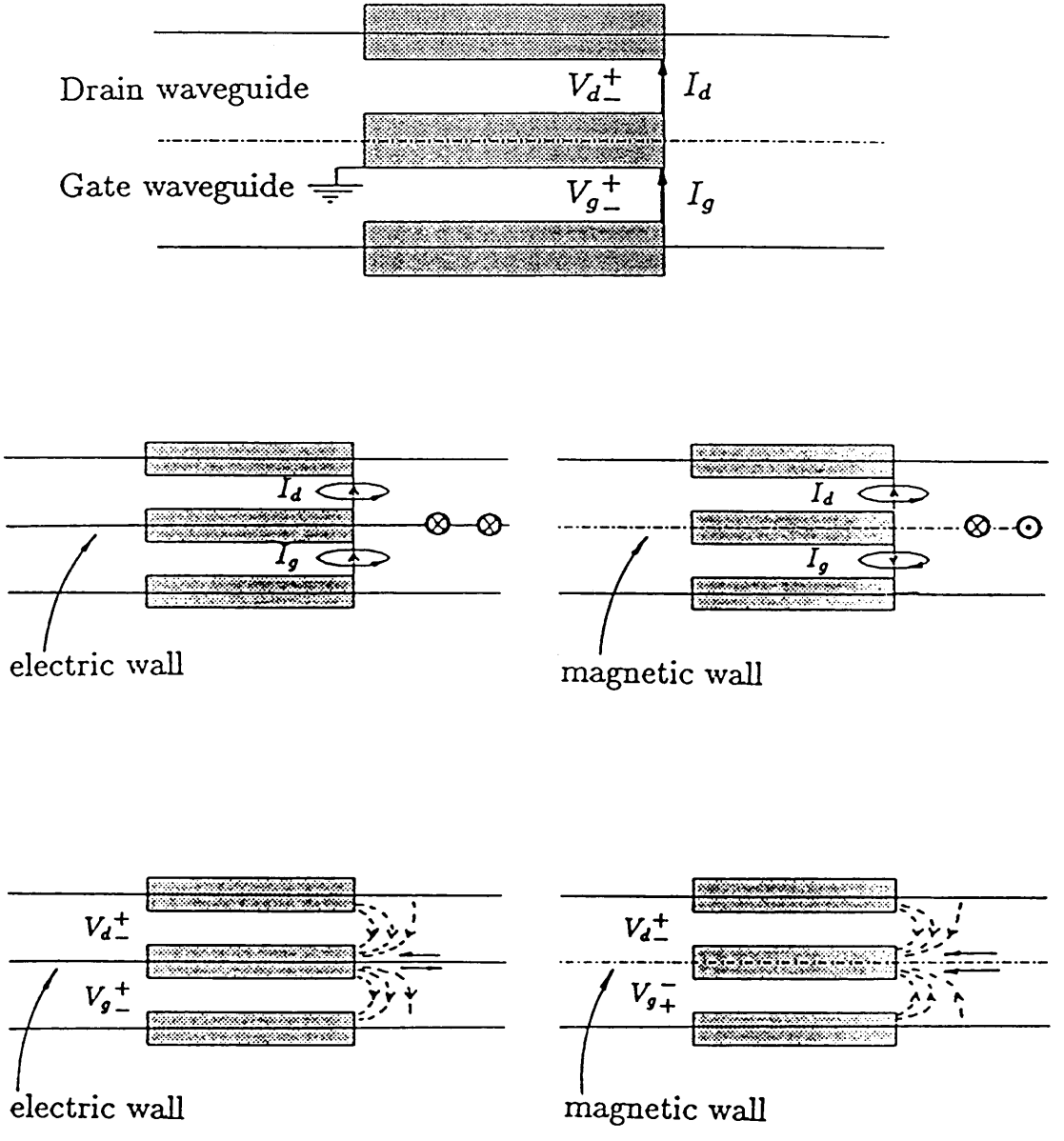


Fig. 3.3. Odd and even current and voltage modes reduce the two-waveguide unit cell to a single step in a waveguide.

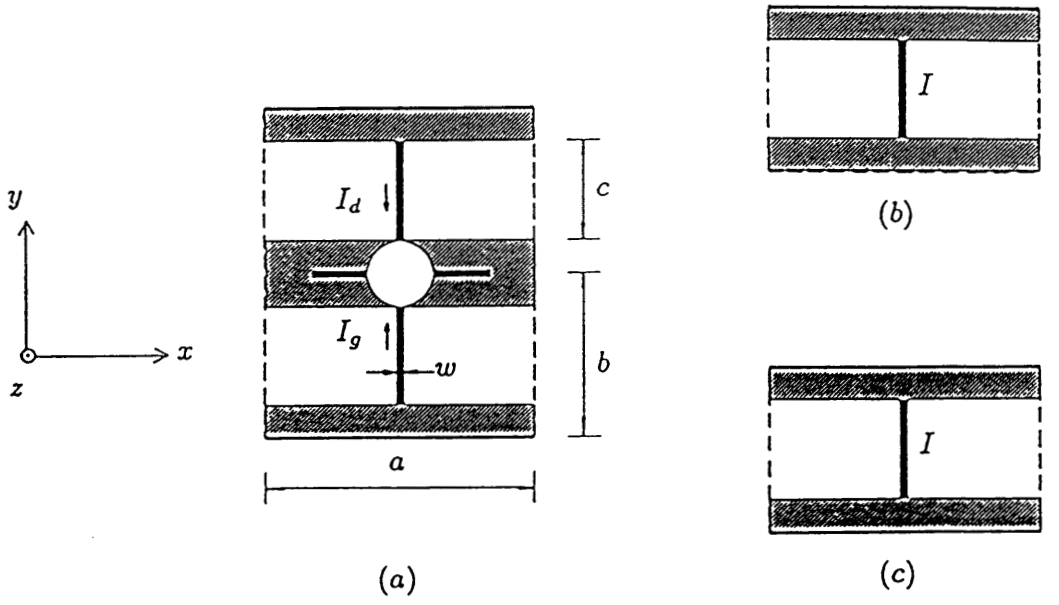


**Fig. 3.4.** The unit cell consists of two waveguides: one excited by the drain current and the other by the gate. Odd and even combinations of the currents reduce the unit cell (a) to (b) and (c), where the electric walls are represented with solid lines, and the magnetic walls with dashed ones.

$$X^M = \sum_{m=1}^{\infty} \frac{\operatorname{sinc}^2\left(\frac{m\pi w}{a}\right)}{\frac{a}{2c} Y_{m0} + \frac{a}{b} \sum_{n=1}^{\infty} Y_{mn} \operatorname{sinc}^2\left[\frac{(2n-1)\pi c}{4b}\right]} \tag{3.1}$$

If one of the currents changes direction, an electric wall can be placed at the symmetry plane (Fig. 3.4c). In this case, the total inductance is given by:

$$X^E = \sum_{m=1}^{\infty} \frac{\operatorname{sinc}^2\left(\frac{m\pi w}{a}\right)}{\frac{a}{2}\left(\frac{1}{b} + \frac{1}{c}\right) Y_{m0} + \frac{a}{b} \sum_{n=1}^{\infty} Y_{mn} \operatorname{sinc}^2\left(\frac{n\pi c}{b}\right)} \tag{3.2}$$

The inductive self-reactance of each lead is the average of the electric wall and magnetic wall reactances, and the mutual inductive reactance is half of the difference of the two:

$$X_s = \frac{X^E + X^M}{2} \tag{3.3}$$

$$X_m = \frac{X^E - X^M}{2}. \tag{3.4}$$

In the formulae above, $a$, $b$, $c$ and $w$ are the dimensions in the unit cell from Fig. 3.2, and $Y_{mn}$ is the $mn$-th mode admittance given by [4]:

$$Y_{mn} = \omega \mu_0 \frac{\left(\frac{2m\pi}{a}\right)^2 - k^2}{\sqrt{\left(\frac{2m\pi}{a}\right)^2 - \left(\frac{n\pi}{b}\right)^2 - k^2}}. \tag{3.3}$$

In a similar fashion, the capacitive self and mutual susceptances are found. These are capacitive reactances that correspond to a step in a rectangular waveguide [4]. They are given by

$$B_s = \frac{a}{b} \sum_{\substack{n=1 \\ n \text{ odd}}}^{\infty} Y_{0n} \operatorname{sinc}^2\left(\frac{n\pi c}{4b}\right) \tag{3.4}$$

$$B_m = \frac{a}{b} \sum_{\substack{n=1 \\ n \text{ odd}}}^{\infty} Y_{0n} \operatorname{sinc}^2\left(\frac{n\pi c}{4b}\right) - \frac{a}{2b} \sum_{\substack{n=2 \\ n \text{ even}}} Y_{0n} \operatorname{sinc}^2\left(\frac{n\pi c}{2b}\right). \tag{3.5}$$

## 3.2 Equivalent Circuit for the Bar-Grid Oscillator

The equivalent circuit for the transistors in the grid is shown in Fig. 3.5. The center-tap transformer describes the coupling into free space. The center tap is the common source bar. The effect of the mirror from Fig. 3.1 is represented as a shunt reactance. The parameters at the 3 GHz operating frequency, with $a = 10\,\text{mm}$, $b = 5\,\text{mm}$, $c = 3\,\text{mm}$, and $w = 0.75\,\text{mm}$ are: $Z_{TEM} = 188\,\Omega$, $\theta_{TEM} = 45°$, $X_s = 30\,\Omega$, $X_m = 0.25\,\Omega$, $B_s = 1.33\,\text{mS}$, $B_m = -0.57\,\text{mS}$.

The simulation of the circuit was done with a microwave CAD program called *Puff*, developed at Caltech [5]. The grid is simulated as the one-port from FIg. 3.5 looking into a matched load, as shown in Fig. 3.6a. In this case, the oscillation condition is:

$$s_{grid}\, s_{load} = 1. \tag{3.6}$$

This means that for a matched load ($s_{load} = 0$), the grid reflection coefficient becomes infinite. As the transistors are saturating, $s_{grid}$ loops in the clockwise direction, trying to reach the point at infinity. Since the Smith chart is a bilinear transformation, this can happen if $s_{grid}$ loops in the counterclockwise direction.

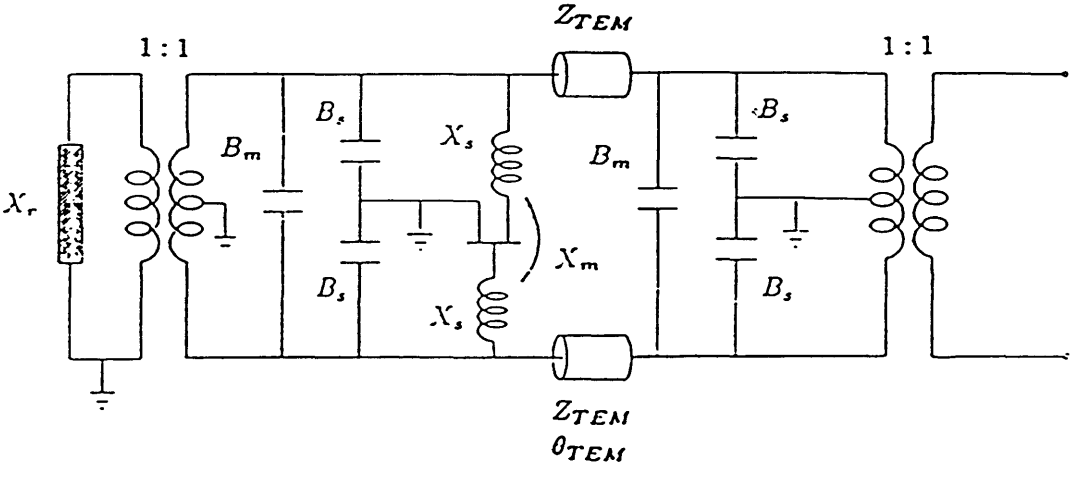


**Fig. 3.5.** Equivalent transmission-line circuit for transistors in the grid.

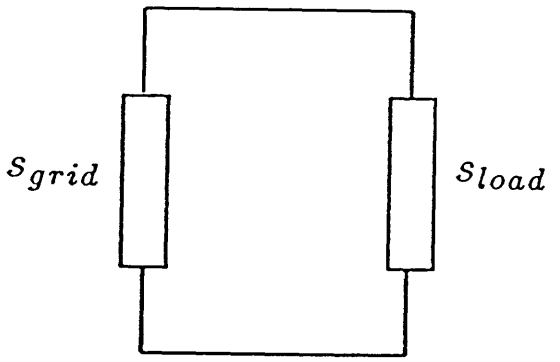


(a)

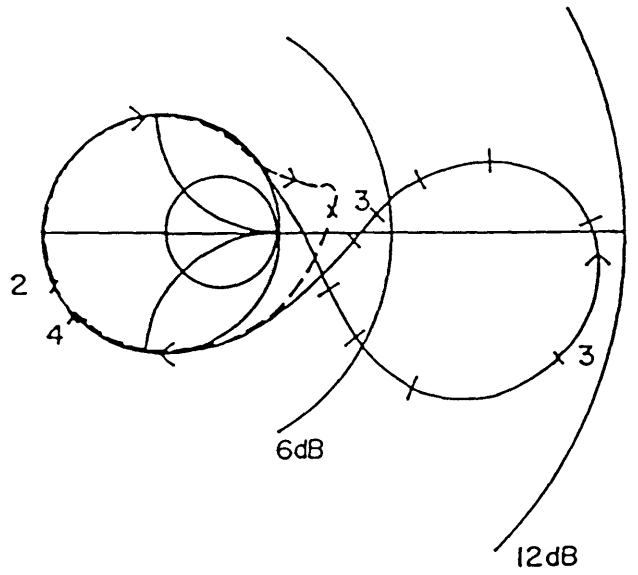


(b)

Fig. 3.6. (a) The oscillator is simulated as a one-port looking into a matched load. (b) Simulation of the transmission-line equivalent circuit. The dashed line shows the circuit behavior when the transistors are not saturated. The solid line shows the saturated behavior with a counterclockwise loop.

So, an instability is manifested as a counterclockwise loop on the Smith chart, and the oscillation frequency occurs where the magnitude of the reflection coefficient is the largest. The simulation predicts an oscillation frequency of 3 GHz, which agrees with experiment. Fig. 3.6b shows the grid reflection coefficient on a Smith chart with a radius of 4 (12 dB). To illustrate this behavior, also plotted on the same Smith-chart is the reflection coefficient with the small-signal transistor $s$-parameters. Saturation in oscillation is simulated by reducing the transistor $s_{21}$ parameter by 3 dB, which shows the counterclockwise loop.

## References

[1] R. L. Rogers, D. P. Neikerk,"Use of Broadside Twin Element Antennas to Increase Efficiency on Electrically Thick Dielectric Substrates," *International Journal of Infrared and Millimeter Waves, Vol. 9, No 11,* 949–971, November 1988.

[2] D. B. Rutledge, S. E. Schwarz, "Planar Multimode Detector Arrays for Infrared and Millimeter-Wave Applications," *IEEE Journal of Quantum Electronics, Vol. QE-17, No.3,* 407–414, March 1981.

[3] R. L. Eisenhart, P. J. Kahn, "Theoretical and Experimental Analysis of a Waveguide Mounting Structure," *IEEE Trans. on Microwave Theory and Techniques, Vol. MTT-19, No. 8,* August 1971, pp. 706–719.

[4] R. F. Harrington, "Time-Harmonic Electromagnetic Fields," *McGraw Hill,* 1961, pp. 171–176.

[5] R. C. Compton, D. B. Rutledge, "*Puff* — Computer Aided Design for Microwave Integrated Circuits," program manual, pp. 26, 1987. Available from the authors.

# Chapter 4

# The Bar-Grid Oscillator — Measurements

## 4.1 Locking and Reliability

The photograph of the 36-MESFET bar-grid oscillator [1] is shown in Fig. 4.1. This grid locks at around 3 GHz, and the measured spectrum is shown in Fig. 4.2. It is stable to within 2 MHz during 24 hours of CW operation. It is not sensitive to vibrations, and this was verified when the antenna pattern of the grid was measured by rotating it in a mount with stepper motors. The grid has an interesting locking sequence that is illustrated in Fig. 4.3. These spectra were

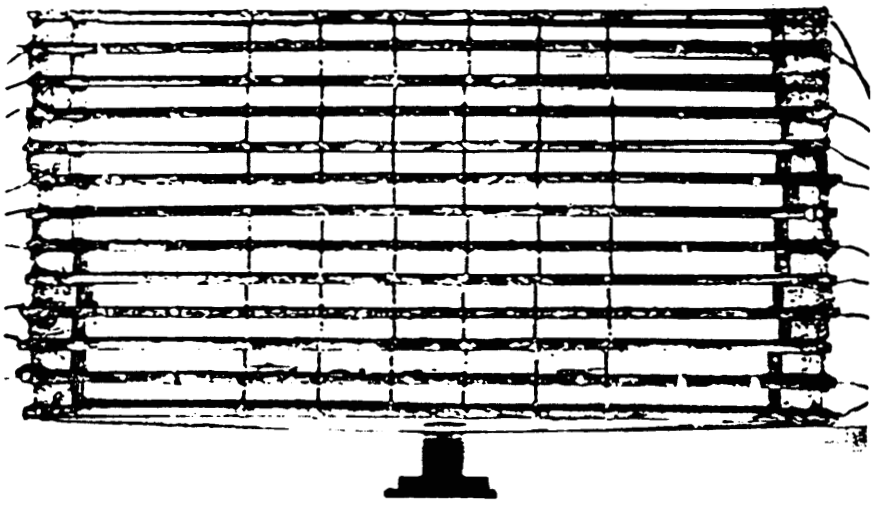

**Fig. 4.1.** Photograph of the 36-MESFET bar-grid oscillator

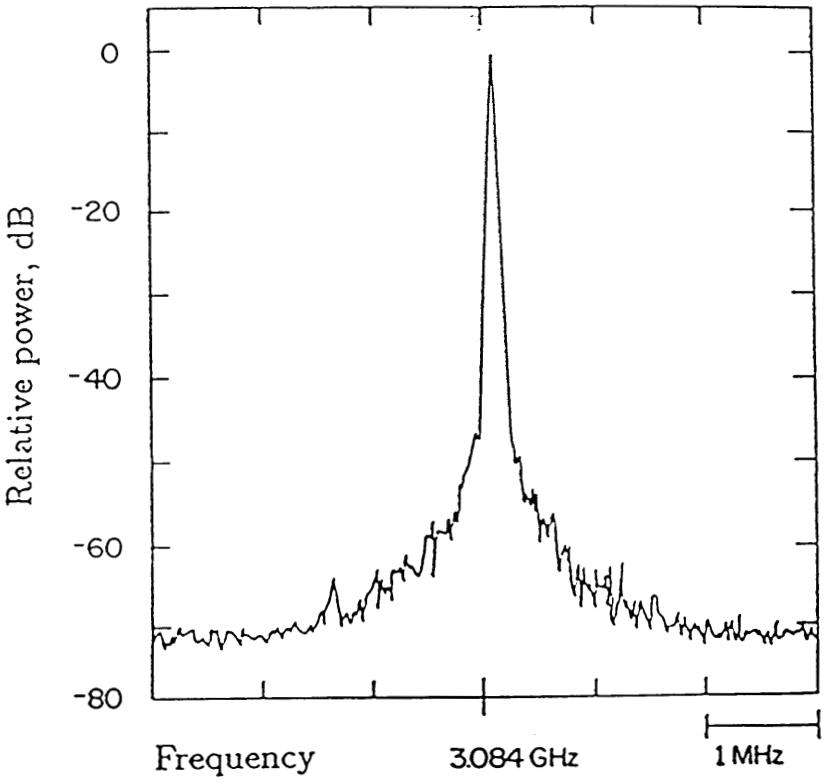


**Fig. 4.2.** Spectrum of a locked 36-MESFET grid oscillator.

recorded as the gate bias was varied over a range of 1 V. Qualitative probing shows that first the devices in individual rows lock, and then adjacent rows lock together. A similar behavior is observed when the mirror position is varied.

The effect of device failures was tested by removing devices indicated in Fig. 4.4a. Fig. 4.4b shows the received power after removing devices labeled according to their position in the grid. The oscillation mode was preserved even when up to 6 out of 36 devices were removed, but the power dropped considerably. The reduction in power should be a much smaller effect when the grid size is increased.

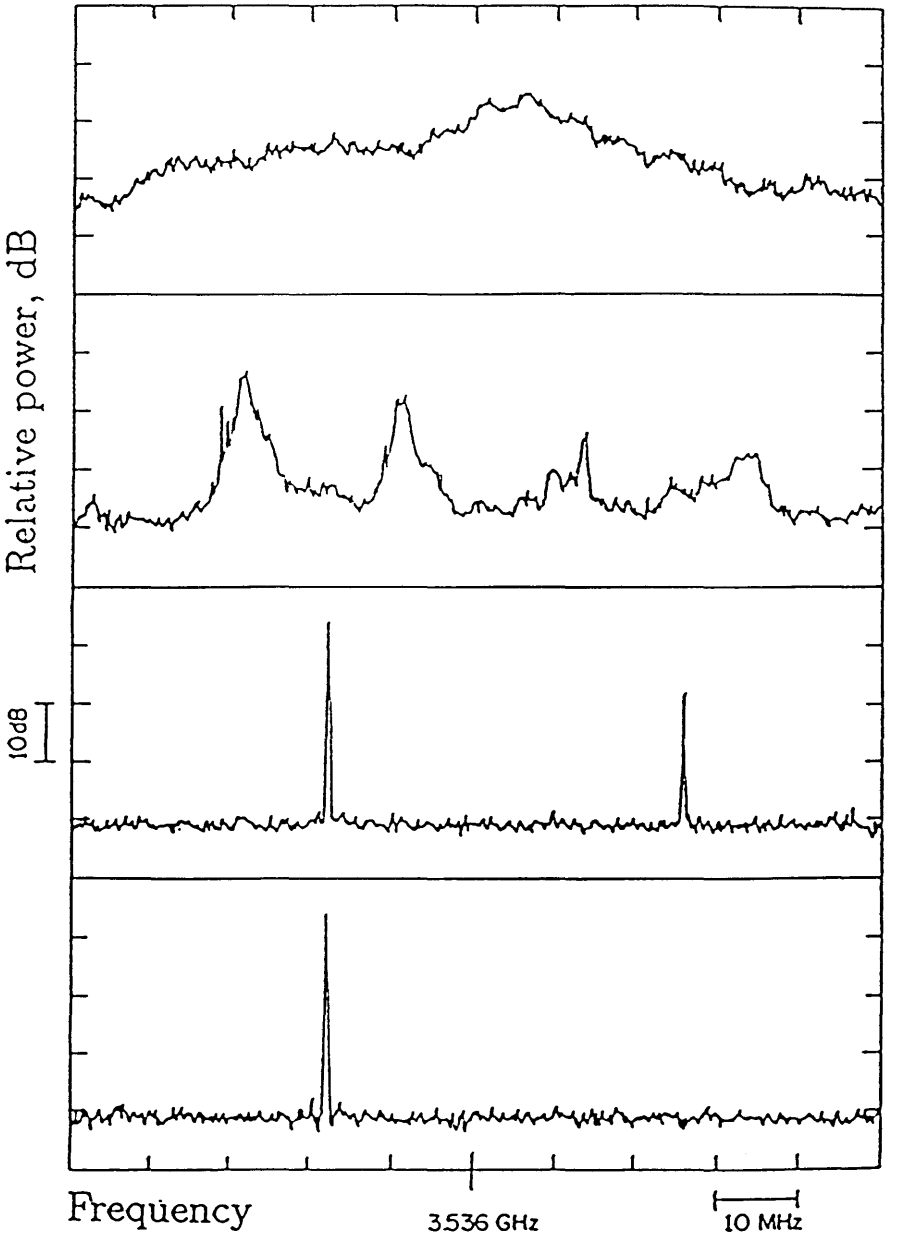


Fig. 4.3. Locking sequence of the oscillator as the gate bias varies.

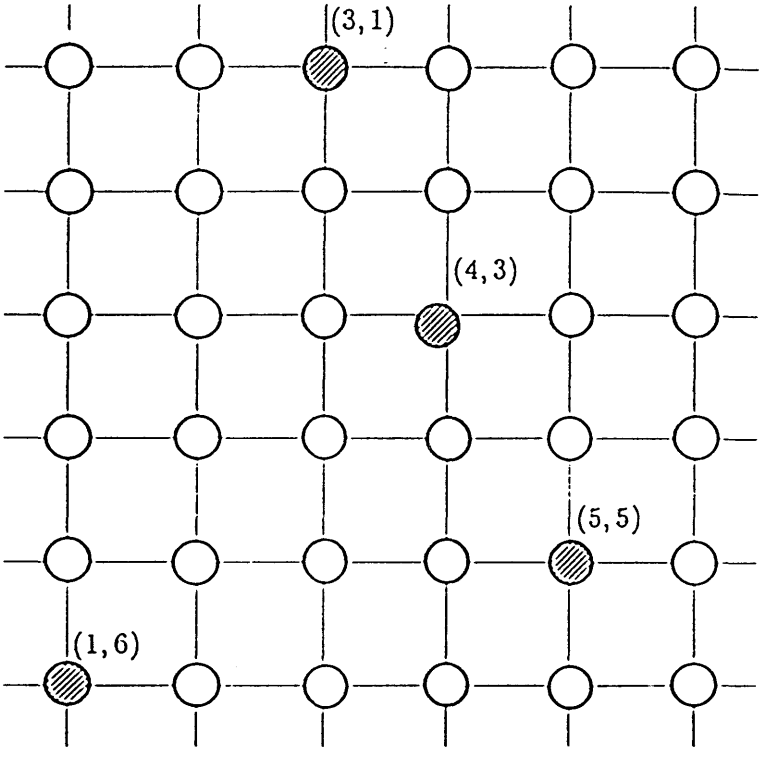


(a)

| Removed devices | $\Delta P$ (dB) |
|---|---|
| (4,3) | −1.5 |
| (5,5) | −2.0 |
| (3,1) | −2.0 |
| (1,6) | −2.0 |
| (1,6), (3,1) | −6.0 |
| (1,6), (3,1), (5,5) | −7.5 |
| (1,6), (5,5), (3,1), (4,3) | −8.5 |

(b)

Fig. 4.4. Grid schematic (a) with removed devices indicated. The table (b) shows the degradation of power as devices were taken out of the grid. The first four rows are for devices removed one at a time, and in the last three they are taken out consecutively.

## 4.2 Power and Pattern Measurements

The bar-grid requires a mirror to lock. When the mirror is very close to the transistors — only 3 mm away — the grid operates in a high-power mode, which is very stable. The power and pattern measurements were made with two dielectric slabs placed in front for impedance-matching. The dielectric constant of the slabs is 12, they are 2 mm thick, and they are placed 20 and 35 mm in front of the grid.

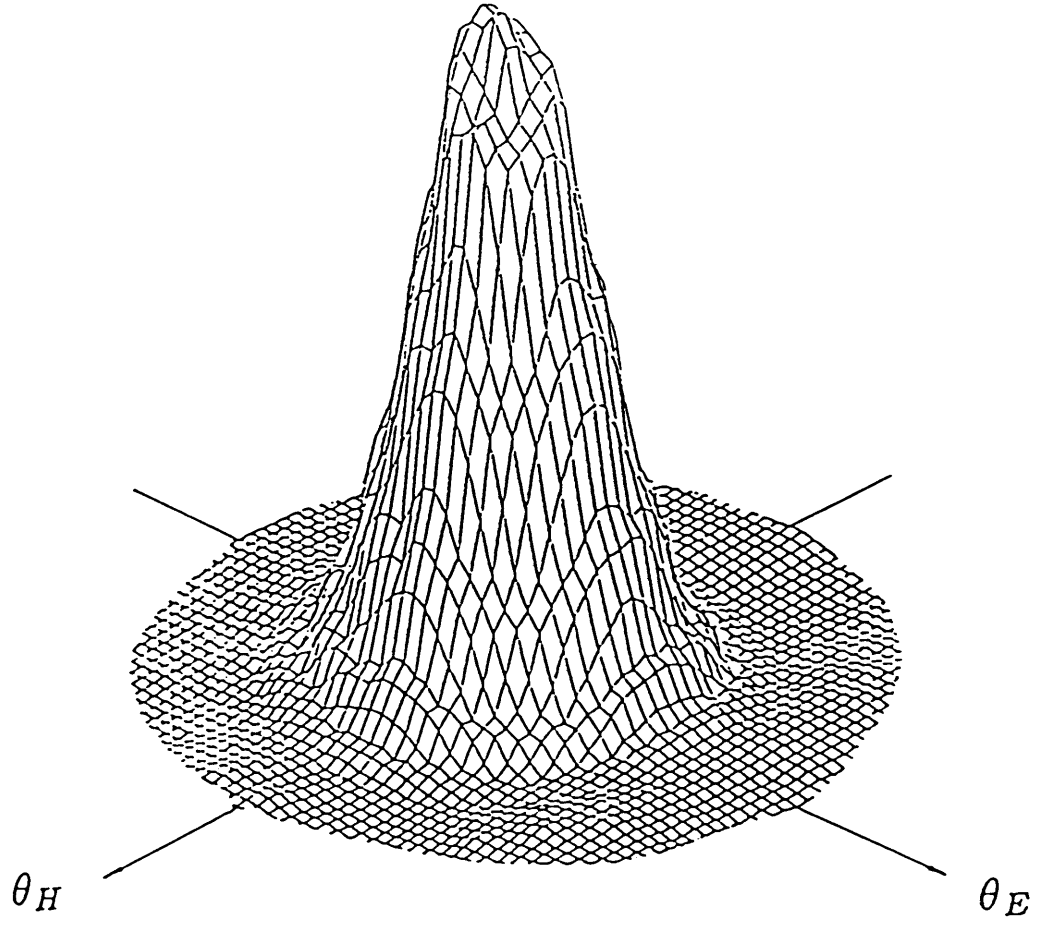


**Fig. 4.5.** Far-field radiation pattern of the bar-grid oscillator. The axes are given in terms of spherical coordinates by $\theta_E = \theta \sin\phi$ and $\theta_H = \theta \cos\phi$. The vertical scale is linear in power.

The far-field pattern of the grid was measured in an anechoic chamber. The mount with the grid fixed to it was rotated with stepper motors controlled by a personal computer. A power meter and a wide-band horn with a 9-dB gain were used to measure the power in the far field (1.5 m away). The measured ERP is 3.0 W. The input DC power is 1.0 W, and the calculated radiated power is 0.22 W. This gives a DC to RF efficiency of 22%, and an isotropic conversion gain of 4.8 dB. The isotropic conversion gain is a concept introduced by Stephan and Itoh [2] and is the product of the efficiency and the directivity.

The measured radiation pattern is shown in Fig. 4.5, and Fig. 4.6 shows the E and H plane patterns (Fig. 4.6a) and the co-polar and cross-polarized patterns (Fig. 4.6b) in the 45° plane. In this mode of operation, the frequency of the grid can be tuned over 300 MHz by translating the mirror (10% tuning bandwidth).

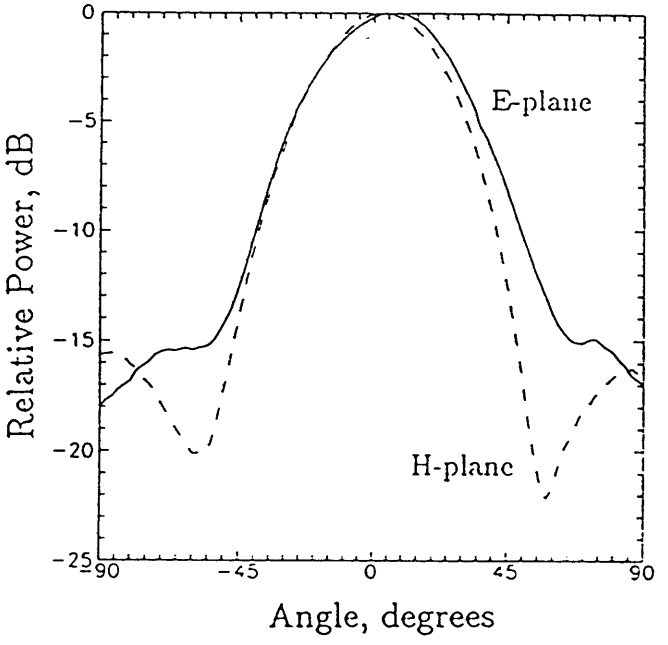


(a)

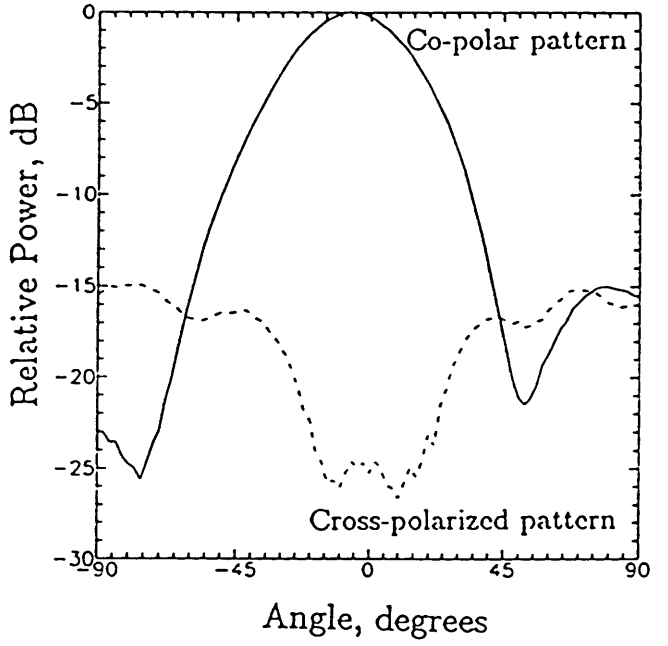


(b)

Fig. 4.6. The E and H plane patterns (a) of the bar-grid oscillator, and the 45° plane co-polar and cross-polarized patterns (b).

## 4.3 Modulation

Another mode of operation at a lower drain current and larger mirror spacing gives lower power, but allows electrical modulation through the bias lines. The gate voltage modulates the frequency over 300 MHz (250 MHz/V). The drain voltage has more effect on the amplitude, so there is a possibility for AM or FM. Fig. 4.7 shows a measured FM spectrum, with a modulation frequency of 5 MHz and a modulation index $\beta$ of 2. The FM spectrum is given by [3]:

$$x(t) = A \sum_{n=-\infty}^{\infty} J_n(\beta) \cos 2\pi(f + nf_m)t. \tag{5}$$

The calculated Bessel coefficients are indicated in Fig. 4.7, and they agree well with the experiment.

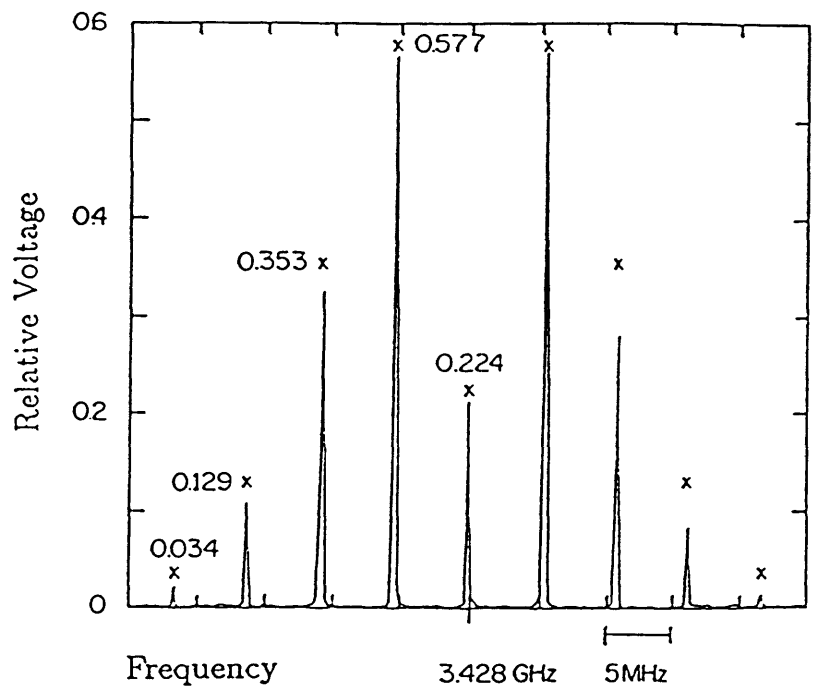


Fig. 4.7. Measured bar-grid oscillator FM spectrum. The scale is linear in voltage and the numbers at the x's give Bessel-function coefficients.

## References

[1] Z. B. Popović, R. M. Weikle, M. Kim, K. A. Potter, D. B. Rutledge, "Bar-Grid Oscillators," *IEEE Trans. on Microwave Theory and Techniques, Vol. MTT-38, No. 3,* 225–230, March 1990.

[2] C. Stephan, T. Itoh,"Planar Quasi-Optical Subharmonically Pumped Mixer Characterized by Isotropic Conversion Loss ," *IEEE Trans. on Microwave Theory and Techniques, Vol. MTT-32, No. 1,* 97–102, January 1984.

[3] R. E Ziemer, W. H. Tranter, "Principles of Communications," *Houghton Mifflin Co., Boston,* 1976, pp. 117.

# Chapter 5

## The Planar Grid Oscillator

The planar grid oscillator is shown in Fig. 1. The transistors are Fujitsu GaAs MESFET's (FSC11), made for satellite receivers at 4 GHz, which typically produce 20 mW in a microstrip oscillator. The devices in adjacent rows share the gate and drain bias lines. The symmetry of the grid forces cancellation of RF currents along the horizontal bias lines, so that the radiation is primarily

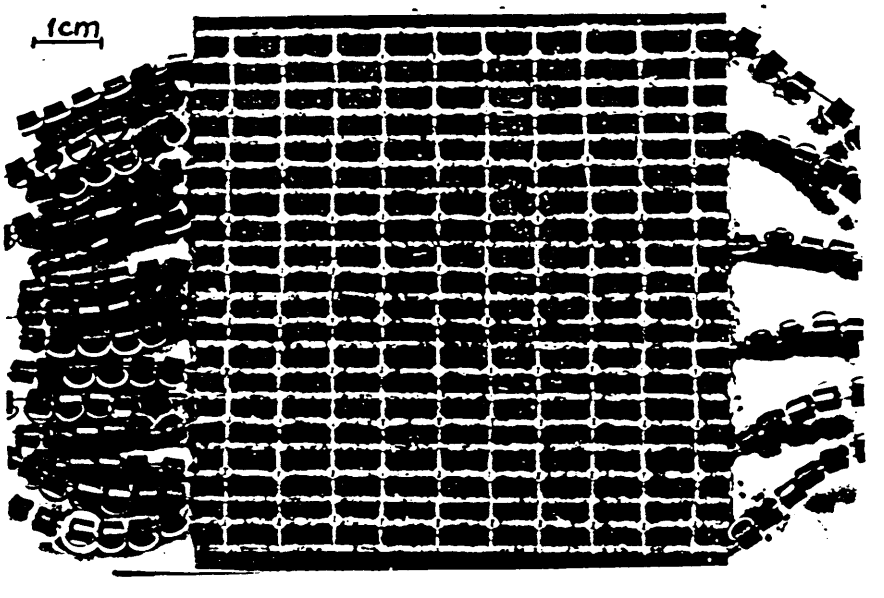


Fig. 5.1. The 100-MESFET planar grid oscillator. The horizontal lines are the bias lines. Ferrite beads are added to the bias lines to suppress lower-frequency oscillations. All the gates, drains and sources are connected, so there are a total of three wires used for the grid bias. The vertical leads are gates and drains, and the radiated electric field is polarized in this direction.

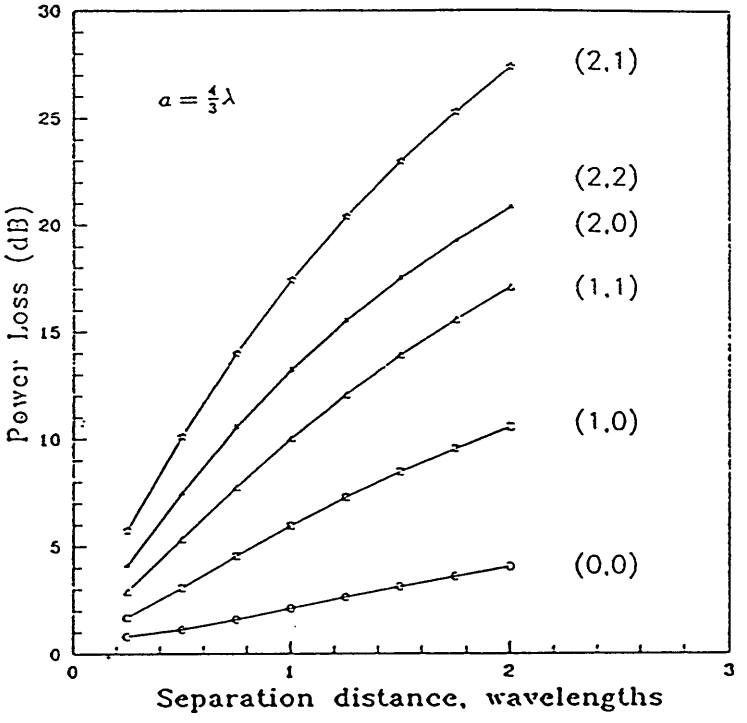


**Fig. 5.2.** Calculated power diffraction loss per round trip for different modes as a function of the cavity length. The dimensions of the cavity correspond to the planar grid oscillator dimensions [3].

from the vertical drain and gate leads. The grid is made on a 0.5 mm thick low-dielectric constant ($\epsilon_r = 2.2$) material on top of a 2.5 mm thick Duroid slab with $\epsilon_r = 10.5$. There is a flat metal mirror behind the grid. The mirror and the grid form a Fabry-Perot cavity about a wavelength long. When the bias to the transistors is turned on, oscillations build up, and all the cavity modes compete. The mode with the lowest diffraction loss per round trip survives, and the devices in the grid lock to this mode.

Analysis similar to that of Fox and Li [2] was done for the case of a Fabry-Perot metal-reflector resonator of the same size as the grid [3]. Fig. 5.2 shows the calculated loss per round trip for different modes. The lowest-order mode has about 2 dB lower loss per round trip than the next mode. This can also be

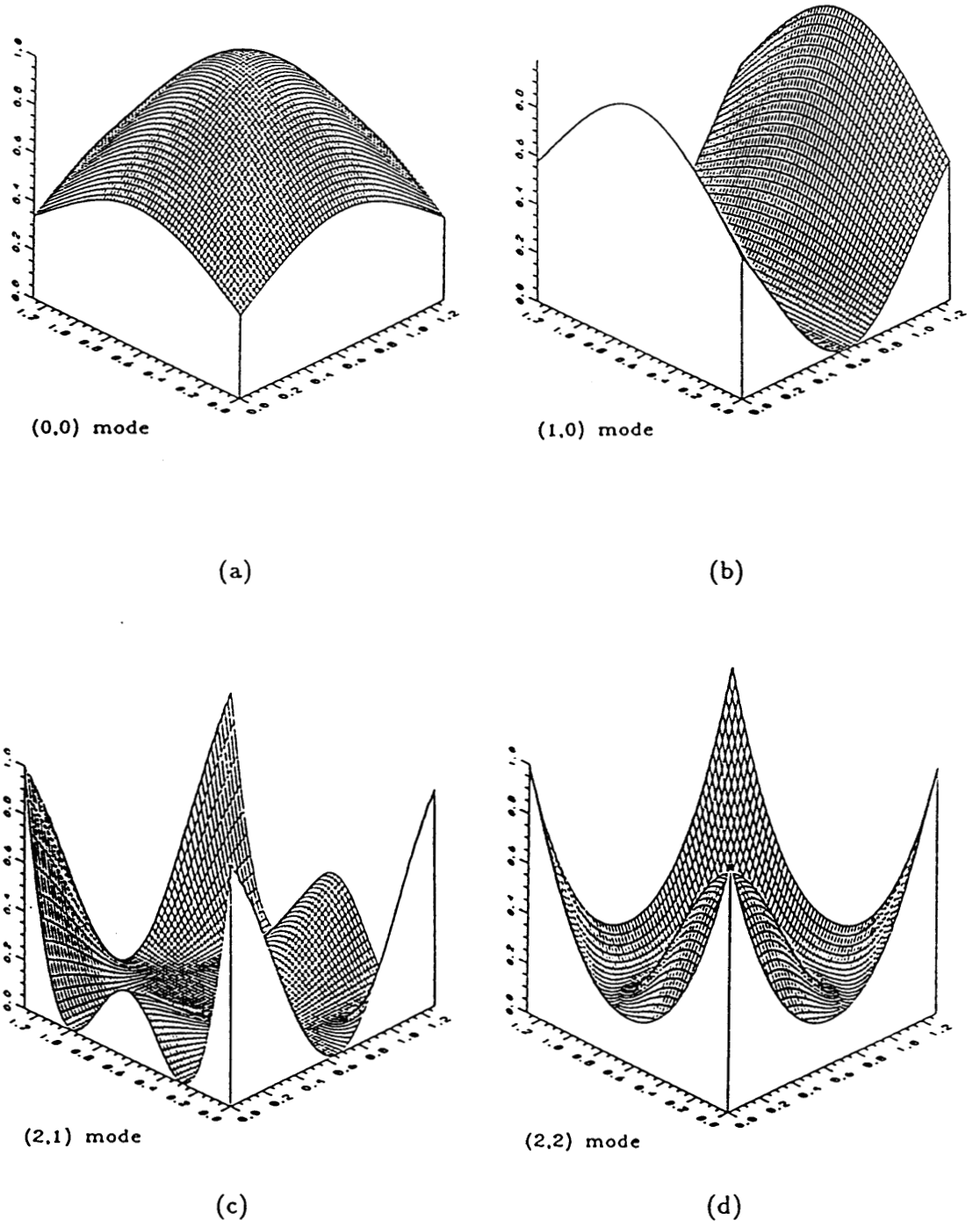


Fig. 5.3. Calculated mode patterns for the (0,0) mode (a), (1.0) mode (b), (2,1) mode (c), and (2,2) mode (d). In the simulations, it typically took ten round trips for the mode to converge [3].

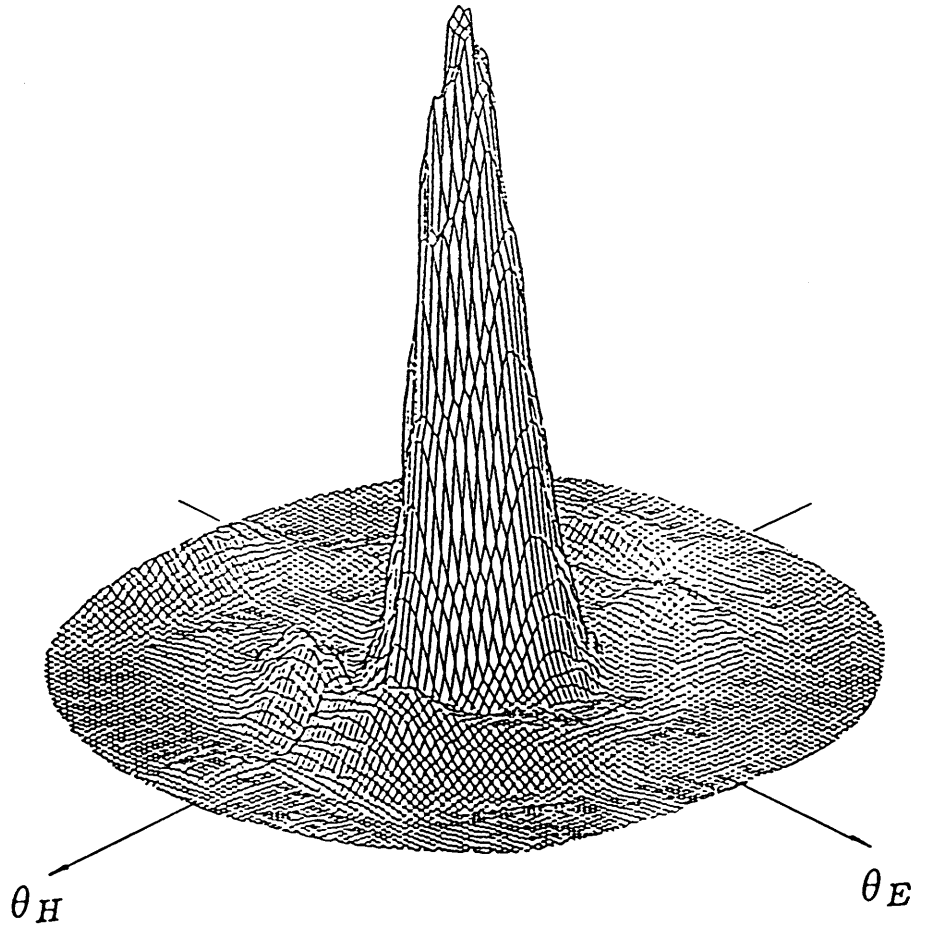


Fig. 5.4. The measured radiation pattern of the planar grid. The vertical scale is linear in power. The axes are given in terms of spherical coordinates by $\theta_E = \theta \sin\phi$ and $\theta_H = \theta \cos\phi$.

This grid locks at 5 GHz, and in Fig. 5.4 is shown the measured pattern with the mirror 57 mm away from the back of the substrate. The effective radiated power (ERP) is 22 Watts, and the directivity 16 dB. The RF to DC efficiency is 20%, and the isotropic conversion gain [8] is 8.5 dB. The cross-polarized component is 30 dB below the co-polar one at the pattern peak.

## 5.1. Equivalent Circuit

In an infinite grid with all the devices locked in phase, symmetry allows us to represent the grid as an equivalent waveguide unit cell. This waveguide has magnetic walls on the sides and electric walls on the top and bottom, as shown in Fig. 5.5. It extends in the $+z$ and $-z$ directions, with the grid in the $z = 0$ plane. The propagating mode is TEM, and the evanescent modes couple to the currents in the transistor leads and present reactive impedances to the device terminals. These reactances can be found by the EMF method [4]. Their values depend on the electrical thickness of the dielectric that supports the grid, on the geometry of the grid, and on the assumed current distribution on the transistor leads. The analysis is similar to that of the bar-grid oscillator described in Chapter 3. A set of TE and TM basis vectors is chosen for the unit waveguide. The currents and fields are expanded in terms of these basis vectors. The power is given by

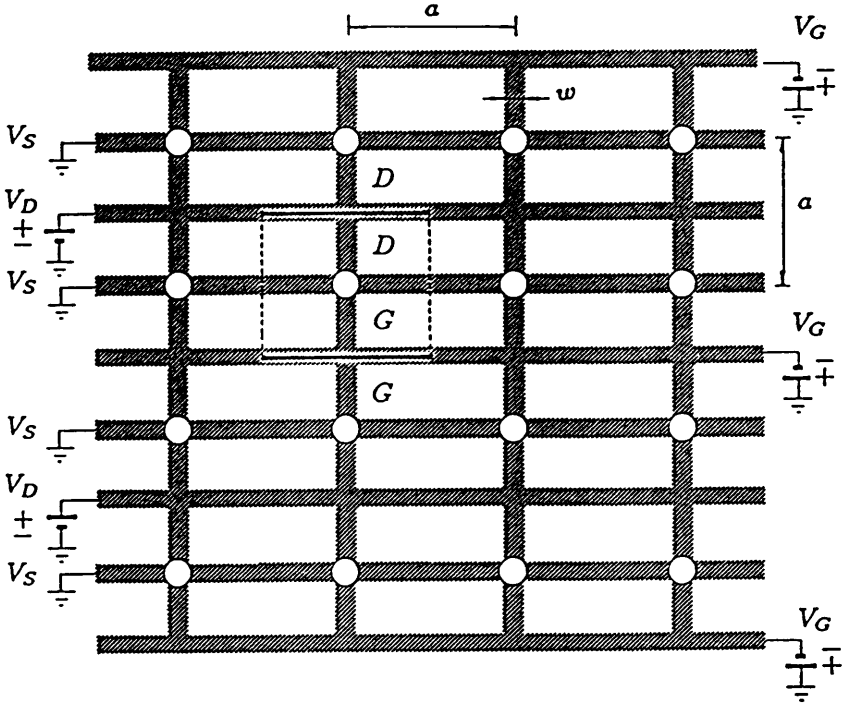


**Fig. 5.5.** Boundary conditions are imposed by the grid symmetry. The solid lines are electric walls ($E_{tang} = 0$) and the dashed lines are magnetic walls ($H_{tang} = 0$).

$$P = \int \vec{E} \cdot \vec{J}\, dS = \sum_{mn} Z_{mn} \left| j_{mn} \right|^2, \tag{5.1}$$

where $j_{mn}$ are the current expansion coefficients for the $m,n$-th mode. $Z_{mn}$ is the parallel combination of the mode impedances in the + and − $z$-direction, and it can include any mirrors or dielectric slabs. The results presented here are derived from a first-order assumption for the currents: A uniform current in the gate and drain leads a linear current in the source lead. The latter is set to zero at the magnetic walls to satisfy the boundary conditions. The current distribution is shown in Fig. 5.6.

The equivalent embedding circuit for the device in the grid is shown in Fig. 5.7. The inductors L in the gate and the drain are the lead inductances. The circuit elements are given by

$$L = \frac{1}{j\omega} \sum_{\substack{m=2 \\ m \text{ even}}}^{\infty} \operatorname{sinc}^2\left(\frac{m\pi w}{2a}\right) Z_{m0}^{TE} \tag{5.2}$$

$$L_S = \frac{1}{j\omega}\left(\frac{2}{a}\right)^2 \sum_{\substack{n\text{odd} \\ m \text{ even}}} \frac{1}{k_{mn}^2} \operatorname{sinc}^2\left(\frac{n\pi w}{2a}\right) \times$$

$$\times \operatorname{sinc}^2\left(\frac{m\pi w}{2a}\right)\left(\frac{m}{n} + \frac{n}{m}\frac{a}{a-w}\right)^2 Z_{mn}^{TE} \tag{5.3}$$

$$C_S{}^{-1} = j\omega\left(\frac{2}{a}\right)^2 \left[\sum_{\substack{n=1 \\ n\text{odd}}}^{\infty} \frac{1}{2k_{0n}^2} \operatorname{sinc}^2\left(\frac{n\pi w}{2a}\right) Z_{0n}^{TM} +\right.$$

$$\left. + 2 \sum_{\substack{n\text{odd} \\ m \text{ even}}} \frac{1}{k_{mn}^2} \operatorname{sinc}^2\left(\frac{n\pi w}{2a}\right) \operatorname{sinc}^2\left(\frac{m\pi w}{2a}\right)\left(1 - \frac{a}{a-w}\right)^2 Z_{mn}^{TM}\right], \tag{5.4}$$

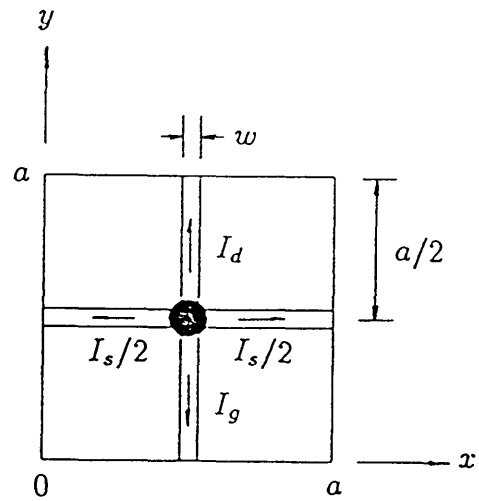


(a)

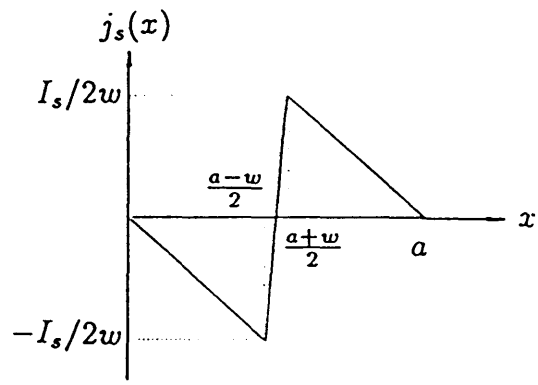


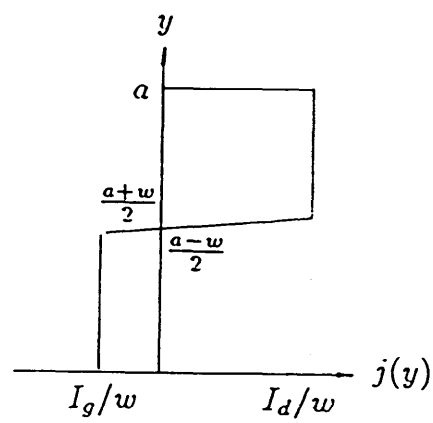


(b) (c)

Fig. 5.6. (a) Transistor in unit waveguide, with source (b) and drain and gate (c) current distributions. The magnitudes of the gate and drain currents are different. The current distribution inside the device is assumed to be linear to avoid discontinuities.

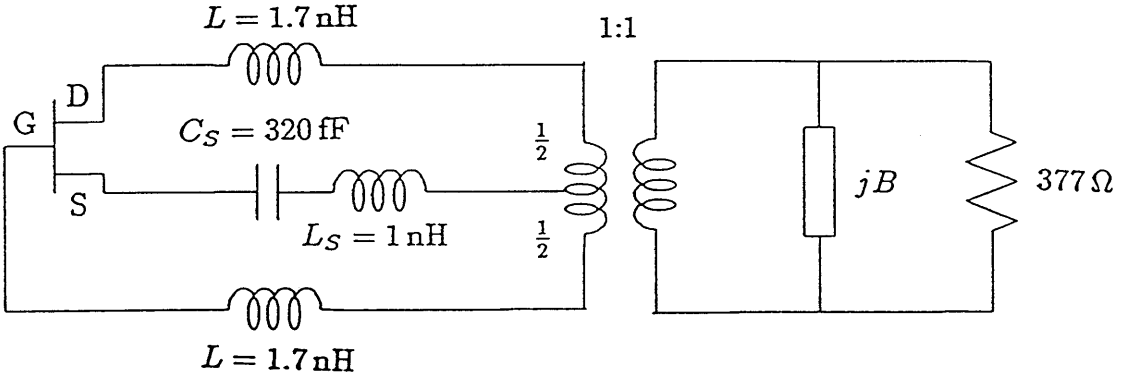


**Fig. 5.7.** The equivalent circuit for a device in an infinite grid. The given reactance values are for the symmetric grid with $a = 8\,\text{mm}$, $w = 1\,\text{mm}$, and a 2.5 mm thick dielectric with $\epsilon = 10.5$.

where $Z_{mn}^{TE}$ and $Z_{mn}^{TM}$ are the impedances of the $mn$-th TE and TM modes [5]. Each of these is a parallel combination of the impedances in the $+z$ and $-z$ directions, and $k_{mn}^2 = (\frac{2\pi}{\lambda})^2 - (\frac{m\pi}{2a})^2 - (\frac{n\pi}{2a})^2$. The transformer describes coupling into free space, which is represented as a $377\,\Omega$ transmission-line. The mirror is represented as a shunt reactance $jB$.

The entire grid is in this way reduced to a one-port equivalent. The measured small-signal transistor $s$–parameters were used, and saturation is taken into account by reducing $|s_{21}|$ by 3 dB. The impedance looking into the oscillator from the $377\,\Omega$ load was examined as a function of frequency. When this impedance becomes $-377\,\Omega$, an oscillation should occur, and the model from Fig. 5.7 predicts 4.92 GHz for a mirror distance of 57 mm. The grid oscillates at 5 GHz for this mirror distance.

We tested the equivalent circuit by building two grids with the same dimensions [6], but with shorting strips instead of transistors, as shown in Fig. 5.8a and 5.8b. The substrates are Rogers Duroid 10 cm square, with a nominal dielectric constant of 10.5, copper cladding on the back, and 2.5 mm thick. The equivalent circuits for these two grids, shown in Fig. 5.8c and 5.8d, use the same

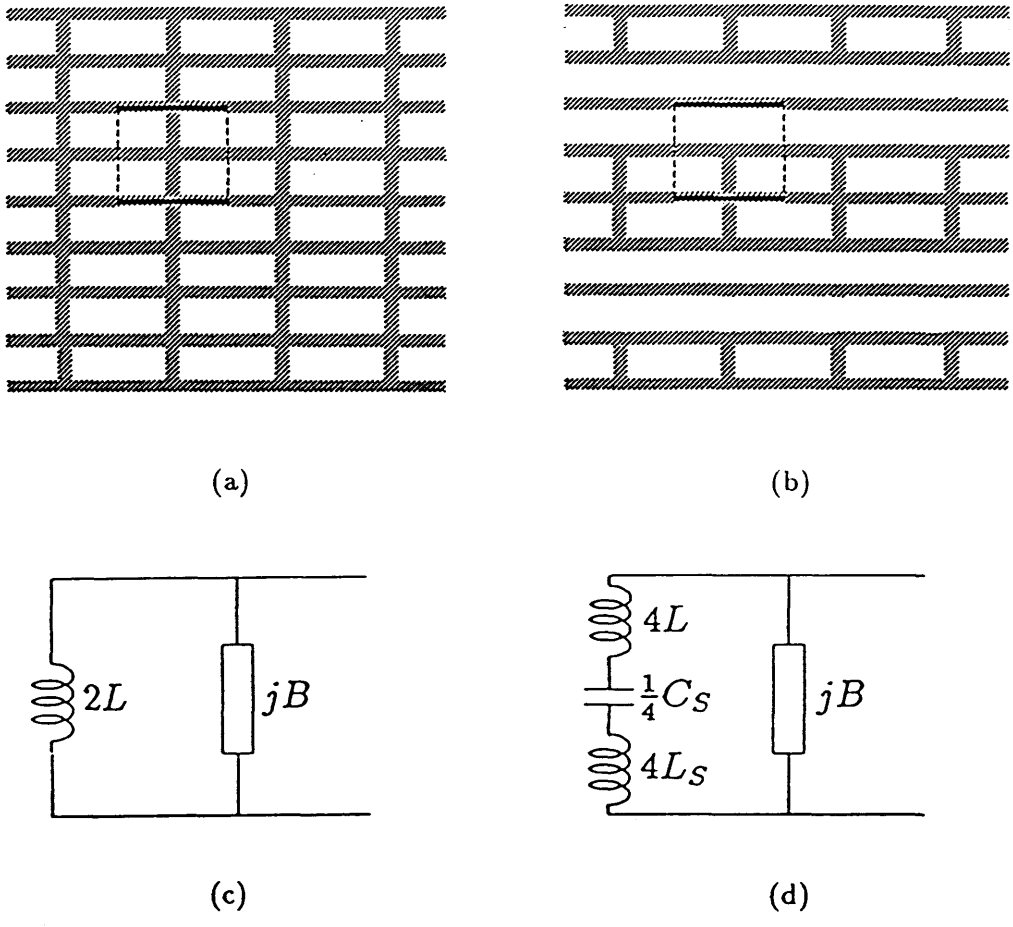


**Fig. 5.8.** Inductive (a) and capacitive (b) grids made on a 2.5 mm thick dielectric ( Duroid, $\epsilon_r = 10.5$). The dimensions of the unit cell are the same as for the MESFET grid. Equivalent circuits for the inductive (c) and capacitive (d) grids.

formulas for inductances and capacitance as the transistor grid. The phase of the reflection coefficient of the grid was measured from 2 GHz to 18 GHz in an anechoic chamber with a wide-band horn and an HP 8510 network analyzer. The calibration was quasi-optical. Microwave absorber at a 45° angle served as the matched load, and a copper sheet as a short. The copper sheet was translated to provide a delayed short as the third standard. The reflection-coefficient phases are shown in Fig. 5.9a and 5.9b. The theoretical phase calculated from the

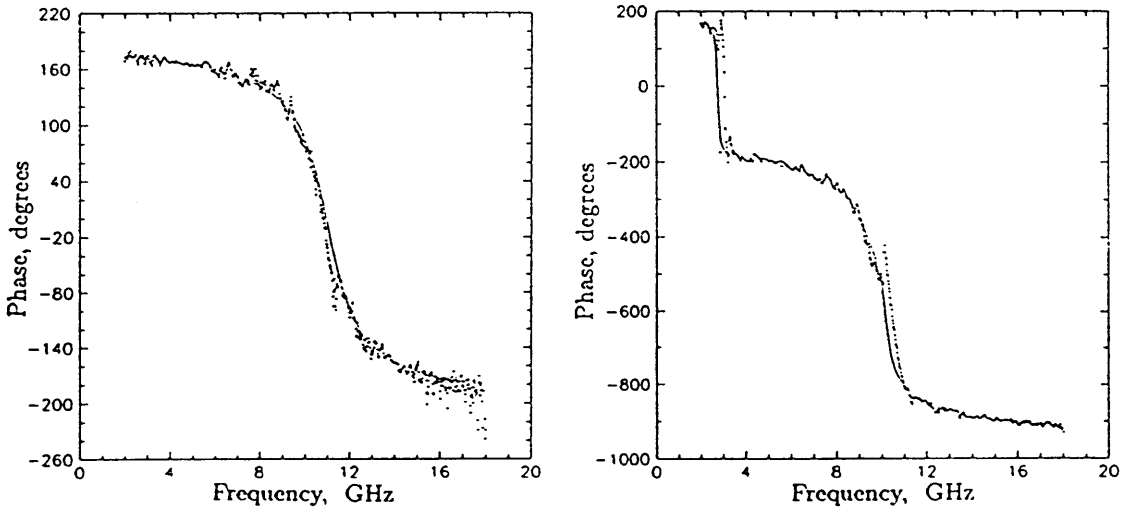


(a) (b)

**Fig. 5.9.** Measured (dashed line) and theoretical (solid line) phase of the reflection coefficient for the inductive grid (a) and capacitive grid (b). Note that the two phase scales are quite different.

equivalent models is shown in solid line for comparison. The substrate electrical thickness is used in the model was measured by stripping the grid pattern and repeating the reflection-phase measurement. The close agreement between theory and experiment gives us confidence in the equivalent circuit model.

## 5.2. Mirror tuning

The position of the mirror has a strong effect on the frequency of oscillation, the grid output power, and the radiation pattern. The equivalent circuit in Fig. 5 predicts frequency tuning as a function of the mirror position. In this simple transmission-line model, the oscillation frequency does not change if the mirror spacing is increased by $\lambda/2$, as shown in solid line in Fig. 8a. The experimental results, shown with dots, agree with the theory. The mirror position affects the width of the main lobe and the size of the sidelobes, as shown in Fig. 9a and 9b. The pattern of the grid is found as that of a uniform array of short dipoles on an infinite dielectric and with an infinite mirror in the back [7]. The distances at which the theory predicts similar patterns are several millimeters larger than seen in the experiment. For some mirror distances, the pattern has a null in the middle, which will prevent locking and will correspond to the region where the grid does not lock.

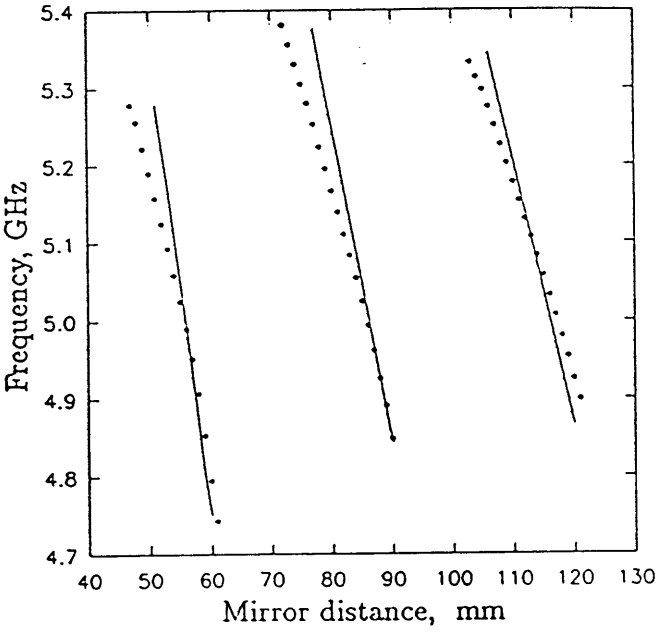


(a)

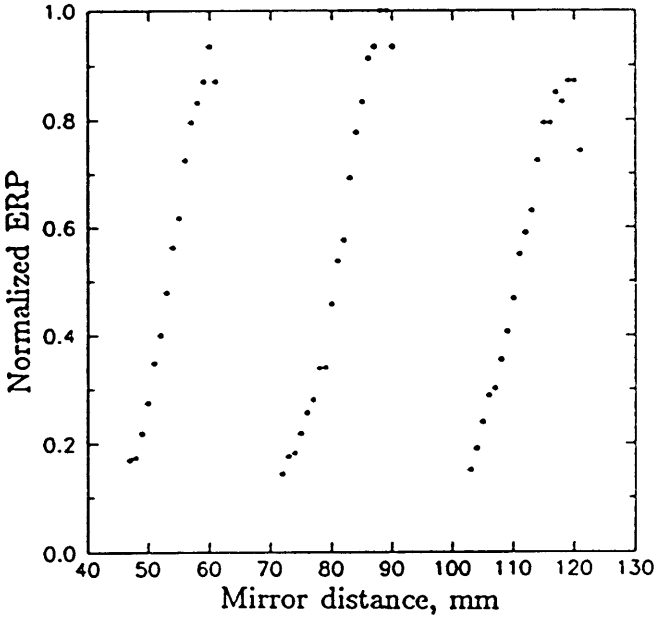


(b)

**Fig. 5.10.** The simulated (solid line) and measured (dots) frequency (a) and power (b) mirror-tuning of the grid.

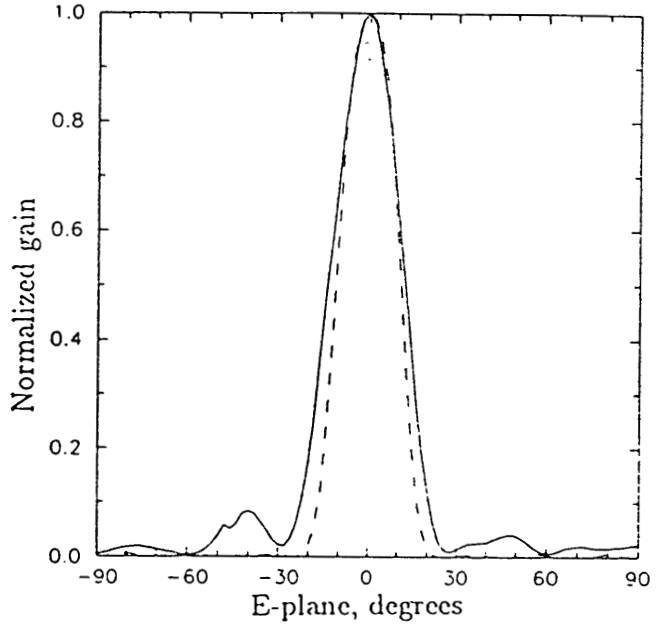


(a)

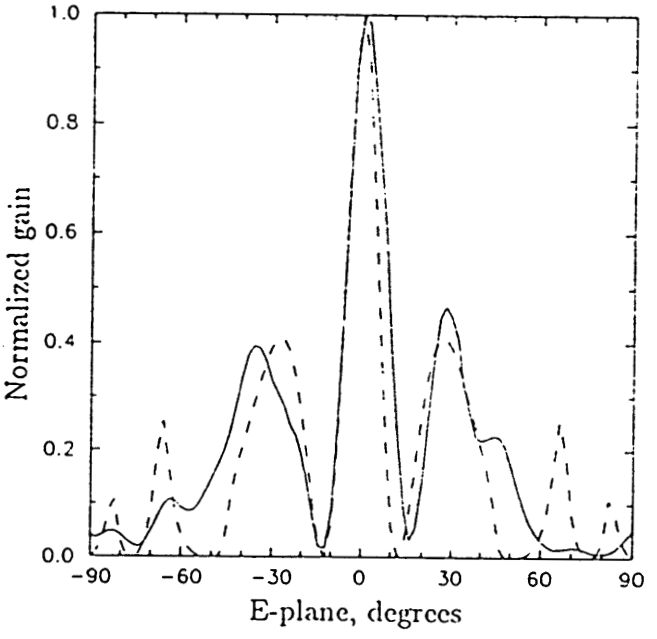


(b)

**Fig. 5.11.** Experimental (solid line) patterns for mirror distances of 54 mm (a) and 82 mm (b). Theoretical (dashed line) patterns [3] for mirror distances of 62 mm (a) and 88 mm (b).

## References

[1] Z. B. Popović, R. M. Weikle, M. Kim, R. D. Rutledge, "A 100-MESFET Planar Grid Oscillator," *submitted to IEEE Transaction on Microwave Theory and Techniques,* April 1990.

[2] A. G. Fox, T. Li, "Resonant Modes in a Maser Interferometer," *Bell Sys. Tech. J., Vol. 40,* 453–488, March 1961.

[3] Moonil Kim, private communication.

[4] R. L. Eisenhart, P. J. Kahn, "Theoretical and Experimental Analysis of a Waveguide Mounting Structure," *IEEE Trans. on Microwave Theory and Techniques, Vol. MTT-19, No. 8,* 706–719, August 1971.

[5] R. F. Harrington, "Time-Harmonic Electromagnetic Fields," *McGraw Hill., New York,* 1961, pp. 349.

[6] Robert M. Weikle, II, private communication.

[7] D. B. Rutledge, D. P. Neikerk, D.P. Kasilingam, "Integrated Circuit Antennas," *Infrared and Millimeter-Waves, Vol. 10,* 1–87, 1983.

# Chapter 6

## Injection-Locking of the Planar Grid Oscillator

In the measured results presented so far, the MESFET's were locked together with no external locking signal present. For some applications it is convenient to be able to lock the devices to an externally injected signal. For example, an electrically modulated low-power oscillator can frequency-modulate the source. The injected signal can also stabilize the frequency, as shown in Fig. 6.1. The injection-locking was performed quasi-optically, as shown in Fig. 6.2. The mea-

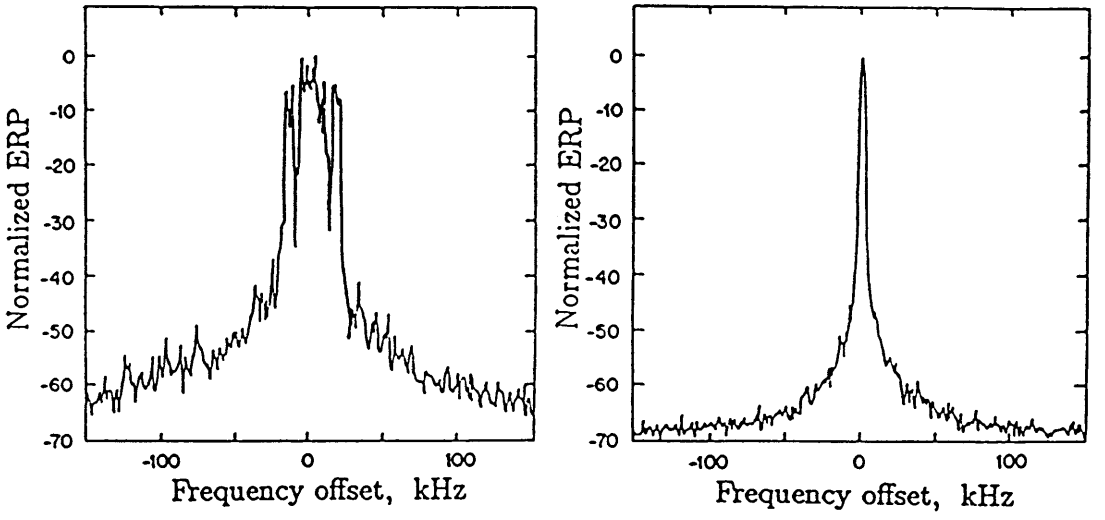


(a) (b)

**Fig. 6.1.** The free-running (a) and injection-locked (b) grid spectra. The center frequency is 5.2 GHz.

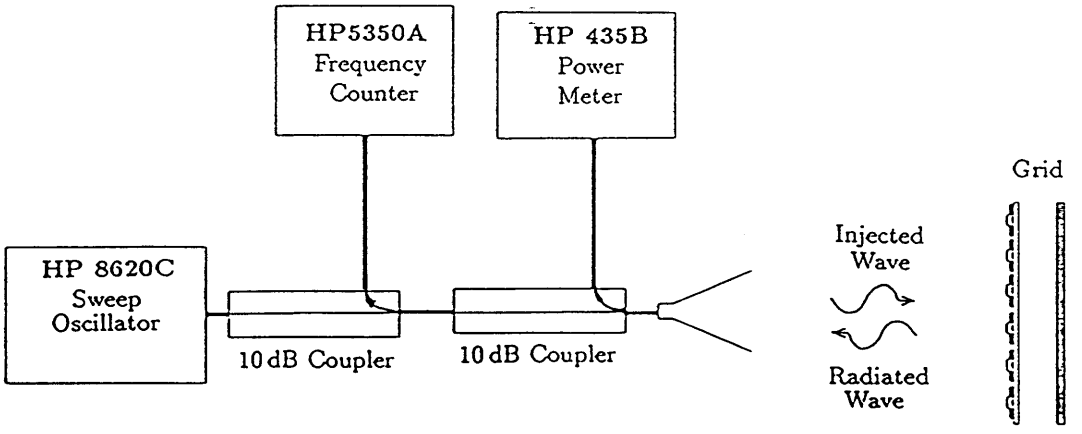


Fig. 6.2. Quasi-optical injection-locking measurement setup.

sured injection-locking bandwidth as a function of the relative injected power is shown in Fig. 6.3, and it is proportional to the square root of the injected power, or, equivalently, to the injected field magnitude, as expected [4].

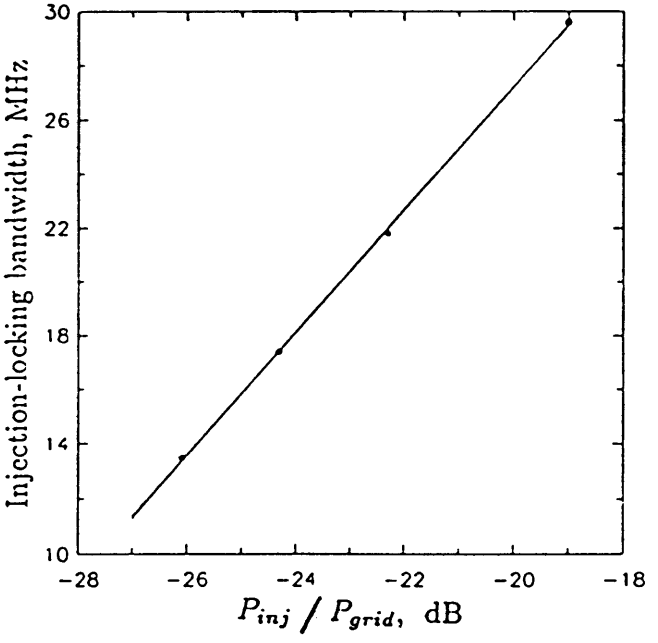


Fig. 6.3. The dependence of the grid locking range on the power ratio of the injected and free-running signal for a mirror distance of $D = 54\,\mathrm{mm}$.

## 6.1. Injection-Locking Theory

Previous injection-locking analysis [4] is based on the assumption that the device impedance is a function of the amplitude only, and that the load impedance is a function of frequency. For the grid, the impedance is a function of both power and frequency, while the load, which is free space, is independent of power and frequency. This suggests a different approach. We use the equivalent circuit shown in Fig. 6.4a. The grid is represented by a reflection coefficient $s_g(p, f)$, which is a function of the transmitted power $p$ and frequency $f$. Free space is represented by a load with a reflection coefficient of zero. The radiated signal is represented by a wave amplitude $a$, where the magnitude of $a$ is the square root of the radiated power. The injected signal is written as $c$, where the magnitude of $c$ is the square root of the injected power. From the circuit model we can write the relation

$$s_g(p, f) = a/c. \tag{6.1}$$

Fig. 6.4b is a plot of $\frac{1}{s_g(p,f)}$ in the complex plane. This is a convenient representation, because the origin represents the free-running oscillation condition. The contours of constant power and frequency may be drawn as straight lines in a small neighborhood about the origin. As the frequency varies, the tip of the $c/a$ arrow will trace out a semicircle, provided the injected power remains the same, and that the deviation of the radiated power is small. For a given $|\frac{c}{a}|$, the frequency deviation varies symmetrically around the free-running frequency from $-\Delta f_{max}$ to $+\Delta f_{max}$, where $2\Delta f_{max}$ is the injection-locking bandwidth. The power deviation $\Delta p$ inside the locking range is not symmetrical in general; for example, in Fig. 6.4(b) it grows in the direction of the arrow, reaching the largest value at the contour $\Delta p_{max}$. From Fig. 6.4(b), the frequency and amplitude of an injection-locked oscillator are given by

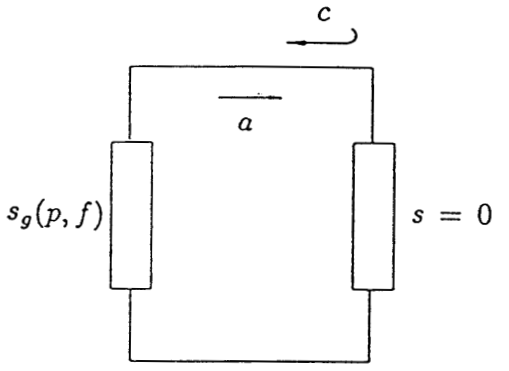


(a)

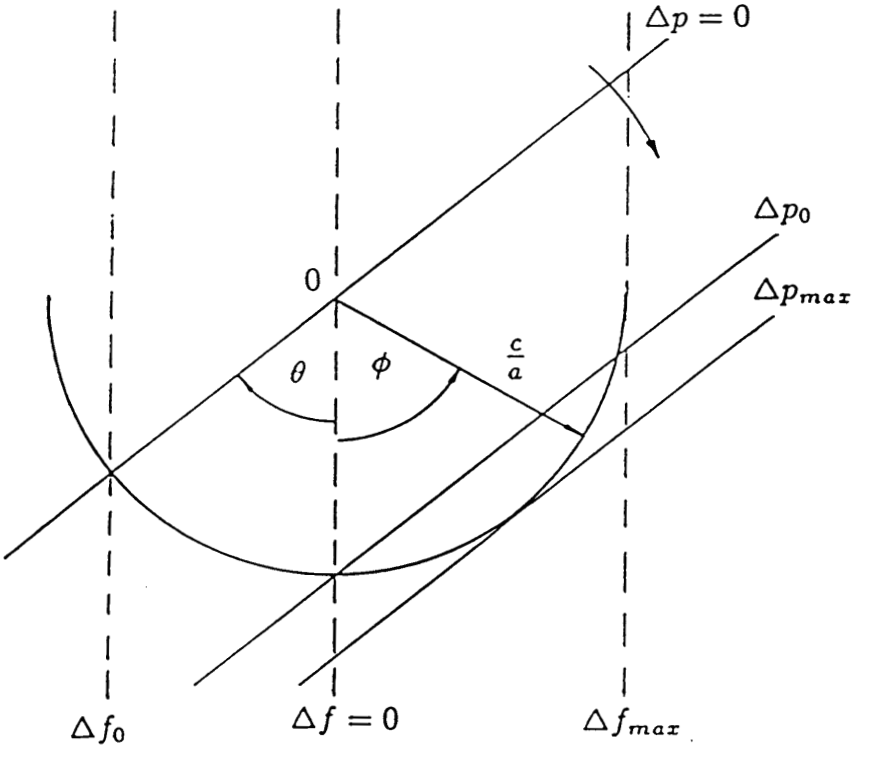


(b)

Fig. 6.4. (a) The equivalent circuit of the injection-locked grid oscillator. $a$ is the power wave radiated from the grid, and $c$ is the injected signal power wave. The reflection coefficient of the grid $s_g(p, f)$ is a function of both power and frequency. (b) Contours of constant $\Delta p$ and $\Delta f$ in the $\frac{c}{a} = \frac{1}{s_g(p,f)}$ complex plane.

$$\Delta f = \Delta f_{max} \sin\phi \tag{6.2}$$

$$\Delta p = \Delta p_{max} \sin(\phi + \theta) \tag{6.3}$$

$$\theta = \arcsin \frac{\Delta p_0}{\Delta p_{max}}, \tag{6.4}$$

where $\theta$ is the angle between the contours of constant $\Delta f$ and $\Delta p$, and $\phi$ changes from $-\pi/2$ to $+\pi/2$ inside the locking range. $\Delta p_0$ is the change in oscillator power at the free-running frequency after it has been injection-locked. This means that it is sufficient to measure $\Delta f_{max}$, $\Delta p_{max}$ and $\Delta p_0$ in order to predict the injection-locked oscillator behaviour. Fig. 6.5 shows measured and calculated power variation of the injection-locked grid for two different mirror positions. Fig. 6.4(b) corresponds to the curve in Fig. 6.5(a). Starting from $-\Delta f_{max}$ and moving along the $c/a$ circle, $\Delta p$ is first negative, then crosses the $\Delta p = 0$ contour, grows to its maximum, and finally starts dropping at the upper end of the locking range.

The tip of the $c/a$ arrow traces a whole circle in the complex plane, but only one half of this circle corresponds to stable solutions. The stability of oscillation is discussed in Fig. 6.6. The contours of growing power are indicated with the direction of the arrow. For oscillations in the top half of the circle (Fig. 6.6b), a perturbation $\delta a$ at a frequency $\Delta f$ causes $c/a$ to move from the contour $\Delta p$ to a contour of larger power $(\Delta p + \delta p)$. This corresponds to an unstable oscillation. The same perturbation will cause a decrease in power for stable solutions lying on the bottom half of the circle (Fig. 6.6a). To decide which half of the $c/a$ circle corresponds to stable solutions, we draw a line from $-\Delta f_{max}$ to $+\Delta f_{max}$, and pick the semicircle to which the power-gradiant arrow points. The described analysis can be potentially useful for characterizing noise, since the oscillator noise can be represented as a collection of injected signals of different powers and frequencies. The presented measurements on the injection-locked oscillator

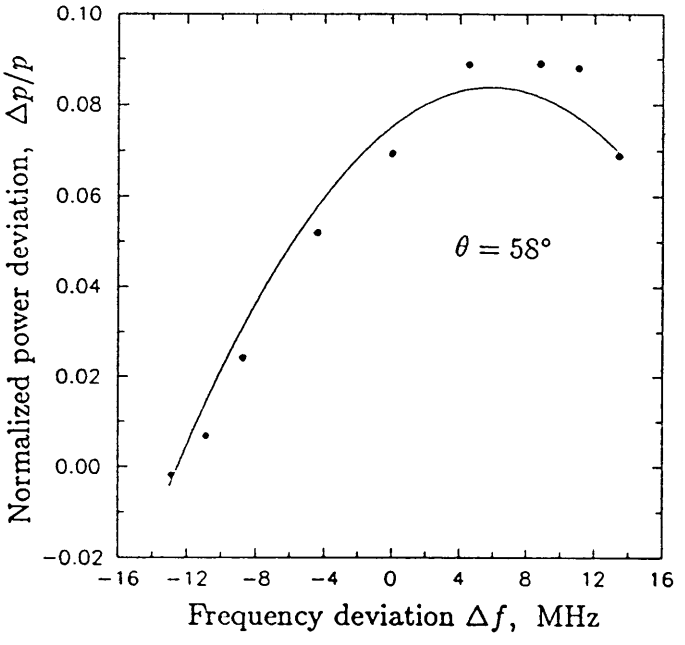


(a)

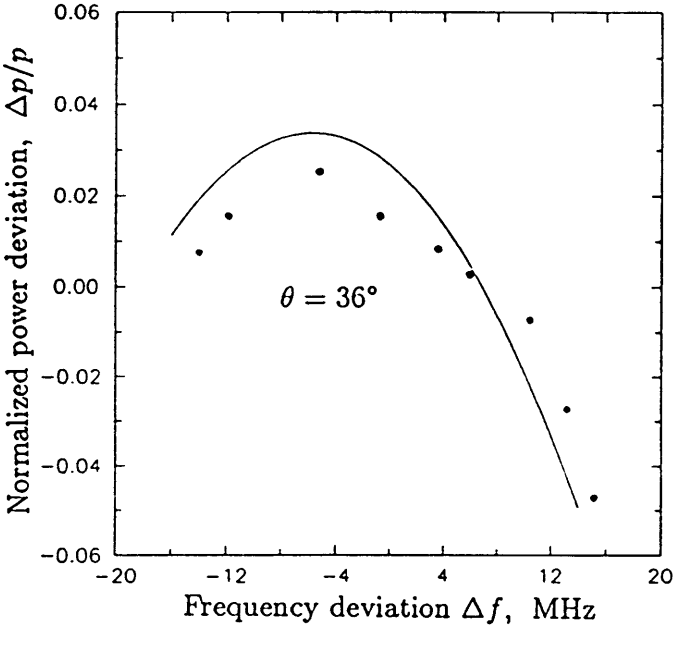


(b)

Fig. 6.5. Variation of the oscillator output power inside the locking range for different mirror positions. The solid lines are calculated from measured values of $\Delta f_{max}$, $\Delta p_{max}$ and $\Delta p_0$.

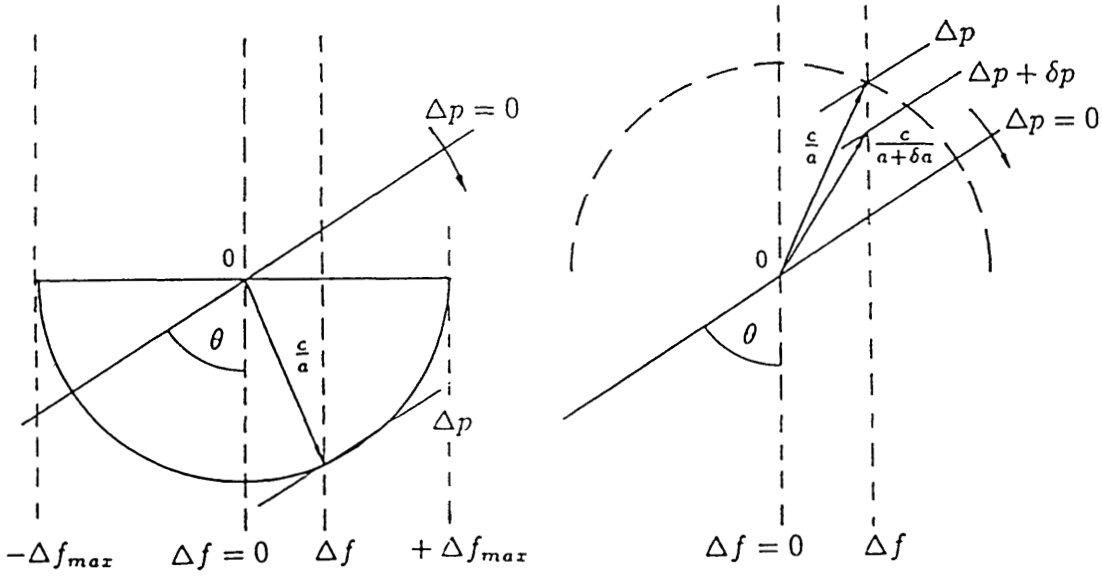


**Fig. 6.6.** Stable oscillations correspond to the bottom half of the $c/a$ circle, and unstable ones to the top half of the circle. The power gradient is in the direction of the arrow.

are scalar measurements. The interesting possibility of measuring contours of constant power and frequency in the $c/a$ complex plane with a vector network analyzer is the subject of future work .

## 6.2. The Grid Oscillator Receiving and Transmitting Patterns

The injection-locking bandwidth of the grid is a function of the incident angle of the injected signal. It is maximum for normal incidence, and decreases sharply as the angle varies from the normal (Fig. 6.7). The pattern is very similar to the transmitting field pattern, which is indicated on the same figure. It might seem surprising that the injection-locking bandwidth has the same pattern as the transmitting grid, but this is actually a consequence of reciprocity. We can understand this by considering a general equivalent circuit for an injection-locked grid, shown in Fig. 6.8. The grid reflection coefficient is $s_g$, and the source of the injection signal has a reflection coefficient $s_i$. The scattering matrix $S(\theta, \phi)$ takes into account the grid pattern, free-space attenuation, and the horn pattern. It is linear, reciprocal and we assume it is matched. The radiated wave from the grid $a_1$ produces a wave $b_2$ in the far field. A wave $a_2$, which feeds the horn from the injection source, produces the injected wave $b_1$ at the grid, so we have

$$b_1 = s_{12}\, a_2 \tag{6.5}$$

$$b_2 = s_{21}\, a_1, \tag{6.6}$$

where $s_{21}(\theta, \phi)$ is effectively the transmitting grid pattern, and $s_{12}(\theta, \phi)$ is effectively the receiving pattern. By reciprocity, these must be equal. From Fig. 6.3, the injection-locking bandwidth is proportional to the injected field magnitude $|b_1|$, which is in turn proportional to $s_{12}(\theta, \phi)$, and to the transmitted wave $|b_2|$. Fig. 6.8 confirms this interesting result.

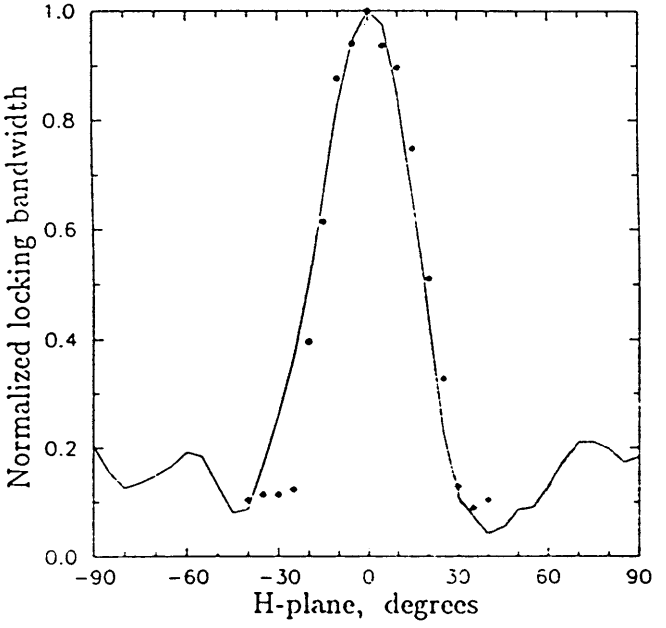


Fig. 6.7. Normalized injection-locking bandwidth (dots) measured as the incidence angle of the injected signal was changed in the H-plane. The solid line shows the measured free-running far-field H-plane pattern. These two curves are the grid receiving and transmitting patterns, and they are closely related by reciprocity. At large angles the injected signal power is not sufficient for locking the grid.

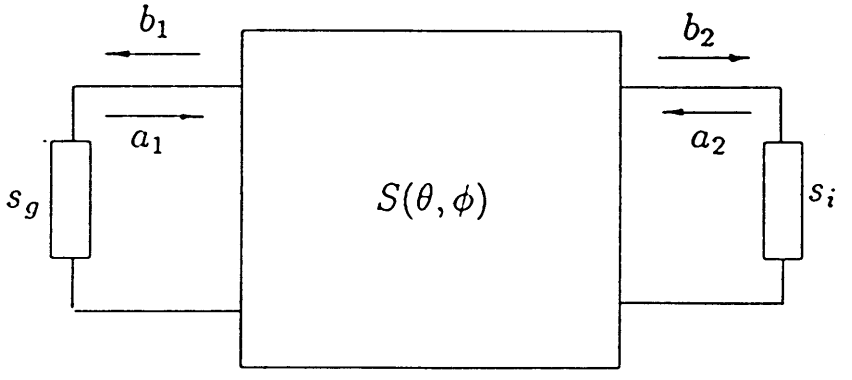


Fig. 6.8. Equivalent circuit for the grid as a receiving and transmitting antenna. The radiated wave from the grid is $a_1$, and the injected wave is $b_1$. The two-port $S(\theta,\phi)$ takes into account the grid pattern, free-space attenuation, and the horn pattern.

## References

[1] Z. B. Popović, R. M. Weikle, II, M. Kim, R. D. Rutledge, "A 100-MESFET Planar Grid Oscillator," *submitted to IEEE Transaction on Microwave Theory and Techniques,* March 1990.

[2] S. Nogi, K. Fukui, "Locking Behaviour of a Microwave Multiple-Device Ladder Oscillator," *IEEE Transactions on Microwave Theory and Techniques, Vol. MTT-33, No. 3,* pp. 253-262, March 1985.

[3] K. Daikoku, Y. Mizushima, "Properties of Injection Locking in the Non-Linear Oscillator," *Int. J. Electronics, Vol. 31, No 3,* 279-292, 1971.

[4] K. Kurokawa, "Injection-Locking of Microwave Solid-state Oscillators," *Proc. IEEE, Vol. 61,* 1386-1410, October 1973.

[5] R. Adler, "A study of Locking Phenomena in Oscillators," *Procedings of the IRE and Waves and Electrons,* 351–357, June 1946.

[6] S. Hamaya, "Stability of the Oscillation Mode in a Multiple-Oscillator System," *IEEE Transactions on Microwave Theory and Techniques, Vol. MTT-33, No. 7,* 593–599, July 1985.

# Chapter 7

## Conclusion and Suggestions for Future Work

The work presented in this thesis demonstrates the feasibility of a high-power, solid-state source at microwave and millimeter-wave frequencies. Experiments on hybrid grid oscillators with MESFET's show that the devices lock to each other and that their power is combined. The oscillators are planar and can be fabricated with the existing semiconductor technology. Any two- terminal or three-terminal devices that have negative resistance at the frequency of interest can be integrated in a grid. Although it can combine thousands of devices, the grid oscillator is a simple structure, since all of the devices share the same biasing and matching circuit. This type of source is especially attractive for millimeter-wave frequencies. In this range the waveguide dimensions become impractically small, and losses in the metal waveguide walls high, so that quasi-optical techniques have many advantages. At higher frequencies, a single wafer is many wavelengths across, so high gains and ERP's can be expected.

Measurements made on the three grids described in this thesis indicate that the grids can be used for a variety of applications. The grid is an antenna as well as a source. In an antenna application, the pattern and ERP would be of interest. In a source application, the power radiated from the grid and the conversion efficiency would be important parameters. The grid is a self-oscillating mixer, so it can be used as a receiver. In this case the noise characteristics and conversion gain need to be determined.

The locking mechanism as well as the power distribution across the grid would be important to investigate. Probing the near fields of the grid and making a field map across the grid surface could prove to be a useful tool for designing future grids. A field picture recorded at different stages of the locking process could help in the understanding of the locking mechanism of such a large number of oscillators.

## 7.1 Scaling

Since the devices in the grid are closely spaced compared to a free-space wavelength, the entire grid can be viewed as a continuous active sheet. In this case, the scaling properties of the grid will be related to its area in wavelengths. The directivity is proportional to the area. The radiated power is proportional to the number of devices, i. e., to the area as well. This means that the ERP grows as the square of the area. In any application where the power is used in the far field, the total power radiated, as well as the directivity is of interest, because both contribute to the power density in the far field. In addition, if the noises of the individual devices are uncorrelated, the noise power is proportional to the area. This means that the signal-to-noise ratio (ERP/N) improves as the area of the grid increases.

If the devices are more than a half of a substrate wavelength apart, the number of substrate modes in the dielectric will grow. The period of the grid is limited by heat considerations and the device geometry at the lower end, and by efficiency at the higher end. The grids described in this thesis have periods from $\lambda_0/10$ to $\lambda_0/3$, where $\lambda_0$ is the free-space wavelength.

Existing state-of-the-art device technology allows some predictions for future monolithic grids. For a high-power application, a Heterojunction Bipolar Transistor (HBT) grid at 90 GHz on a 100 mm diameter wafer could have an ERP of 800 kWatts. This ERP can be achieved if the devices are 1 mm ($\lambda_0/3$) apart and if each device can give 10 mWatts [1]. This gives a total power of 19 dBW, and the directivity of such an active sheet is 40 dB.

High-power devices like HBT's require good heat-sinking. A combination of the bar grid oscillator and the planar grid oscillator would be convenient. The HBT wafer can be placed against metal bars, which would be the radiator as well as part of the impedance-matching circuit. Bipolar transistors also require

a resistive biasing circuit to prevent thermal runaway. In a hybrid microstrip version of a bipolar transistor grid oscillator, an alternative to using chip resistors is to use a special alumina substrate with two-layer metalization [2] that can be used to fabricate thin film resistors by etching. Two masks are needed to fabricate the grid. The first one defines the whole grid structure together with the bias resistors. The second mask defines the places where the copper is etched away, leaving the second layer exposed. Baking the substrate results in oxidation of this layer, which then becomes resistive, with a surface resistance on the order of 25 $\Omega$.

For a very high-frequency application, quantum-well resonant tunneling diodes can give 1 $\mu$W at 200 GHz [3] with good yields. The directivity of a 100 mm diameter grid is 40 dB. Assuming a 0.15 mm ($\lambda_0/10$) period, the radiated power would be 25 dBm, and the ERP 3 kWatts.

Since the grid oscillator consists of a very large number of devices, the reliability of the oscillator is an important issue. If a device fails as an open ciricuit, and the grid is several wavelengths across, the hope is that the mode will not be affected, as was shown in measurements with the bar grid. If a device fails as a short, it shorts out the whole grid, fusing the rest of the devices. In a monolithic version, fuses should be integrated in series with each device. An important issue is the effect of the failure of devices at different positions in the grid. Future investigation on reliability could be done by probing the near fields of the grid when different devices are taken out of the grid, simulating an open-circuit failure.

## 7.2 The grid as a receiver

The injection-locking experiments described in Chapter 6 also indicate that the grid oscillator is a receiver. Outside the locking range, the free-running and injected signal give mixing products that can be detected as the IF on the bias lines. Since the ferrite beads on the bias wires are a high impedance for IF frequencies, the IF can be taken out differentially, as shown in Fig. 7.1. A wire is pulled through the first ferrite bead on the source bias lines, and its two ends soldered to a coaxial connector. In this way the IF is transformer-coupled to an oscilloscope, as shown in Fig. 7.2. In order to characterize the grid oscillator as a receiver, its noise figure and conversion gain need to be measured.

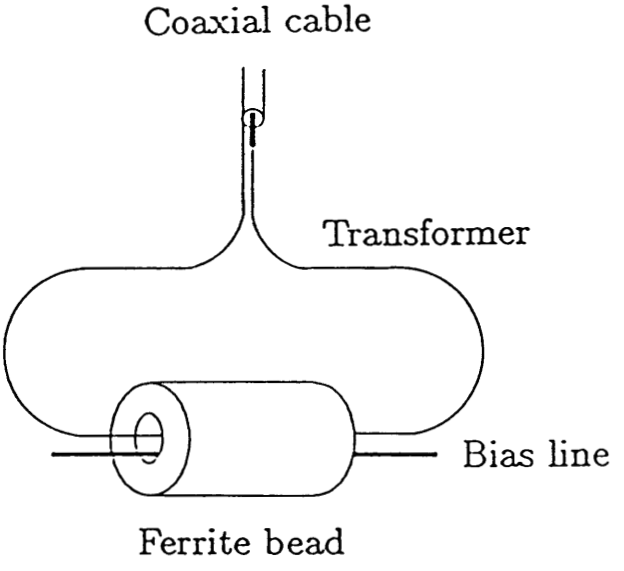


**Fig. 7.1.** Transformer-coupling can be used to detect the IF on the bias lines when the grid is used as a receiver.

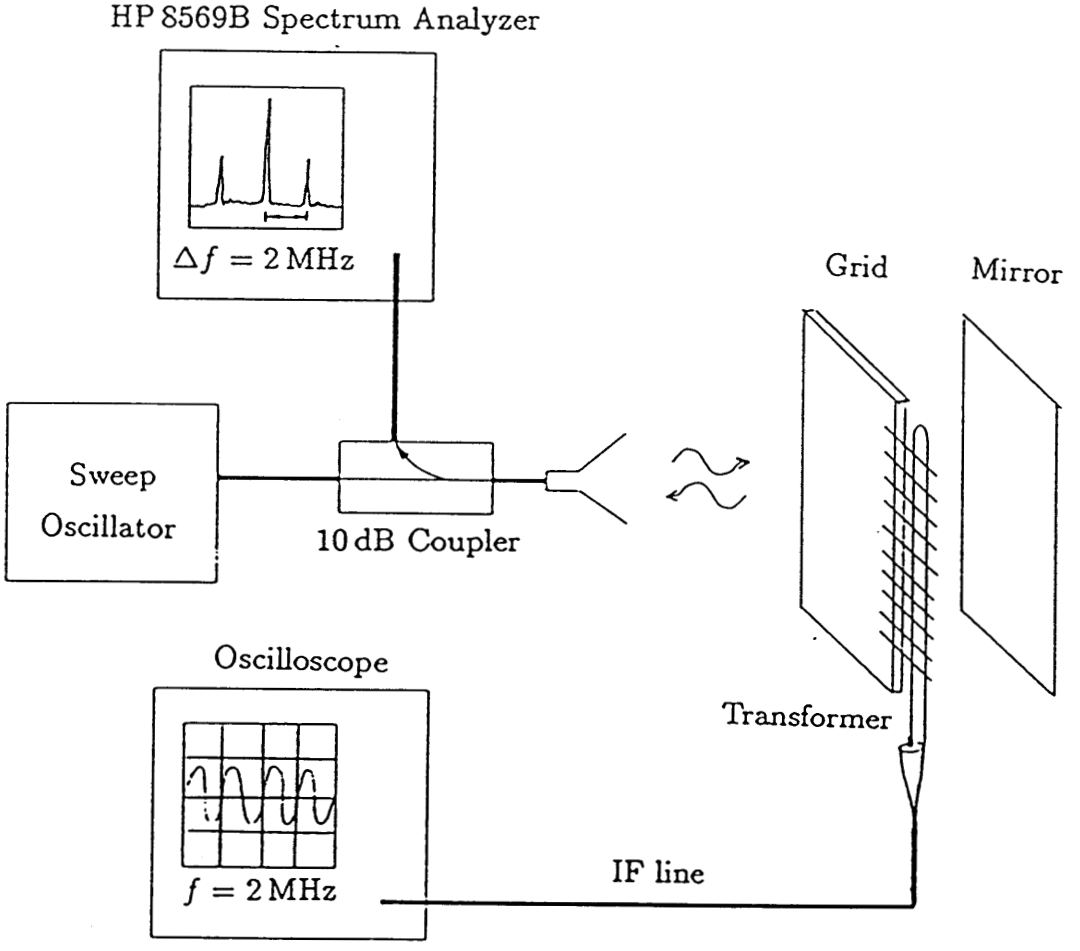


Fig. 7.2. Test setup for the grid as a receiver. The sweeper signal is incident on the free-running grid. The two signals produce an IF, which can be detected on the bias lines.

## 7.3 System Integration

In the previous section several high-frequency grid oscillators with fundamental frequency devices were discussed. An alternative high-frequency grid oscillator can use a subharmonic high-power grid together with a grid of multiplying devices. It is easier to make high-power devices across a wafer with high yield at 30 GHz than it is at 90 GHz. The 30 GHz grid output is incident on a planar grid multiplier [4]. The multiplier can be optimized for a second harmonic oscillator at 60 GHz, or a third harmonic oscillator at 90 GHz. In this case the other harmonics need to be filtered out, and this can be done with passive grids [5]. Such an oscillator can be used as the LO for a receiver. An example of an integrated system is shown in Fig. 7.3. The back-to-back horn array indicated in the figure is a focal plane imaging array [7]. The RF is incident on the front detector array. The LO is brought to the detector from the back side, and the IF circuitry is integrated between the wafers of the front and back array.

The grid oscillator itself is both a transmitter and a receiver, so the grid can be used as a radar. One way to modulate the grid is through the DC bias. For example, if the frequency changes linearly with the gate voltage, as shown for the bar-grid, a sawtooth modulation on the gate DC bias will cause a sawtooth change in the frequency. This is the principle of CW FM ranging radar. The radiated wave and the wave coming back from the target are offset in frequency, and the beat frequency is determined by the range of the target. This beat frequency can be detected on the bias lines.

The frequency can also be modulated mechanically by translating the mirror. In this case the output power changes as well, as described in Section 5.2. The planar grid has a high-power mode and a low-power mode, and the two are offset in frequency by about 200 MHz as shown in Fig. 7.4, which corresponds to Fig. 5.10. The grid can transmit a high-power pulse, and can receive in the low-

power mode. It would be more convenient to do the mirror-tuning electrically. In principle, the mirror can be a grid of bias-dependent reactive devices, such as varactor diodes. By changing the bias of such a grid, the reflection coefficient is varied, and this is similar to changing the position of the mirror. Such a varactor-diode grid is effectively a variable-impedance surface.

Several other applications of the grid oscillator with other grid structures seem attractive. If the grid oscillator main lobe is incident on a phase-shifting surface, the beam can be steered. A monolithic phase-shifting grid at 90 GHz has been demonstrated [8], where the phase of an incident plane wave was shifted by linearly changing the bias on the rows of Schottky diodes across the grid. For some applications, the radiated beam would need to be turned off and on. This can be done without turning off the grid itself. A second grid of switching devices, for example, p-i-n diodes [9], can be placed in front of the grid oscillator

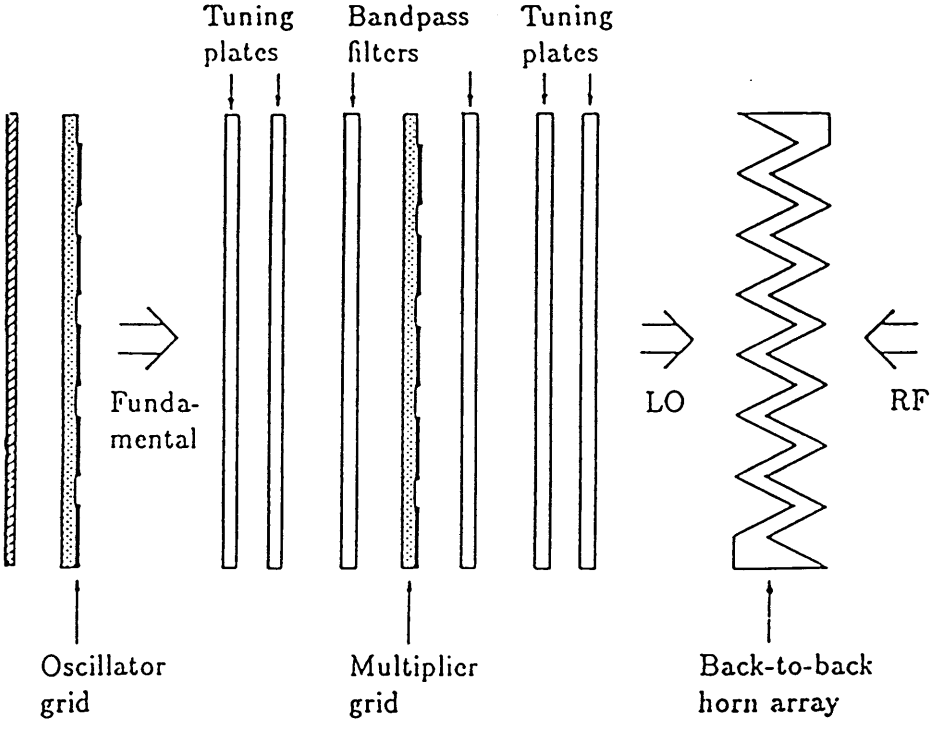


FIg. 7.3. The grid oscillator as the LO in a millimeter-wave imaging-array system.

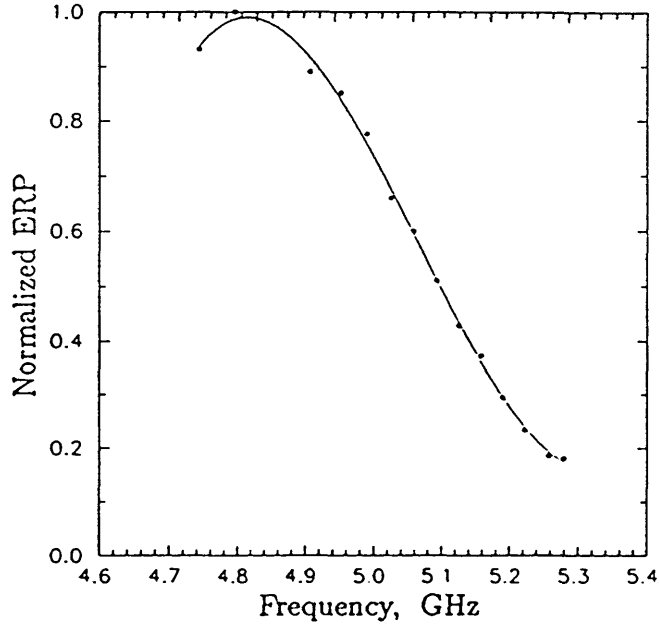


Fig. 7.4. The power variation with of the planar grid oscillator. Both the power and frequency are changed by translating the mirror over 15 mm.

and its transmission coefficient changed electrically. An active-device grid that does not oscillate can be a wave amplifier. In this application the input has to be isolated from the output to prevent positive feedback. One way to do this is to use different polarizations for the input and output waves. For example, if the gate and drain leads were perpendicular in a MESFET grid, the gate would receive one polarization, and the drain would radiate an amplified perpendicularly polarized wave.

In conclusion, the grid oscillator is a planar device convenient for large-scale microwave and millimeter-wave power combining. The quasi-optical approach is easy to implement, and suggests using passive and active grids combined in versatile systems. The work presented in this thesis leads to a number of interesting and useful applications that can be investigated in the future.

## References

[1] P. M. Asbeck, M. F. Chang, K. C. Wang, D. L. Miller, G. J. Sullivan, N. H. Sheng, E. Sovero, J. A. Higgins, "Heterojunction Bipolar Transistors for Microwave and Millimeter-Wave Integrated Circuits," *IEEE Trans. on Microwave Theory and Techniques, Vol. MTT-35,* 1462–1470, December 1987.

[2] Rogers Corporation, "Omega-Ply Clad RT/duroid Laminates," product specification sheet RT 1.99.1.

[3] E. R. Brown, T. C. L. G. Sollner, C. D. Parker, W. D. Goodhue, C. L. Chen, "Oscillations up to 420 GHz in GaAs/AlAs Resonant Tunneling Diodes," *Applied Physics Letters, Vol. 55, No 17,* 1777–1779, October 1989.

[4] C. F. Jou, W. W. Lam, H. Z. Chen, K. S. Stolt, N. S. Luhmann, D. B. Rutledge, "Millimeter-Wave Diode-Grid Frequency Doubler," *IEEE Trans. on Microwave Theory and Techniques, Vol. MTT-36, No. 11,* 1507–1514, November 1988.

[5] J. A. Arnaud, F. A. Pelow, "Resonant-Grid Quasi-Optical Duplexers," *The Bell System Technical Journal, Vol. 54, No. 2,* 263–283, February 1985.

[6] R. J. Hwu, N. C. Luhmann, Jr., C. F. Jou, M. Kim, Z. B. Popović, and D. B. Rutledge,"Array concepts for solid-state and vacuum microelectronics for millimeter-wave generation," 1st International Vacuum Microelectronics Conference, Williamsburg, Virginia, June 1988.

[7] Yong Guo, private communication.

[8] W. W. Lam, C. F. Jou, H. Z. Chen, K. S. Stolt, N. S. Luhmann, D. B. Rutledge, "Millimeter-Wave Diode-Grid Phase Shifters," *IEEE Trans. on Microwave Theory and Techniques, Vol. MTT-36, No.5,* 902–907, May 1988.

[9] A. Armstrong, S. Parisi, C. M. Howell, "High-Power Waveguide Diode-Array-Switch Element," *MSN & CT,* 8–19, November 1987.